A coupled approach for Rolling Contact Fatigue cracks in the Hydrodynamic Lubrication regime: the importance of fluid/solid interactions

Robbie Balcombe[a], Mark T. Fowell[a], Andrew V. Olver[a], Stathis Ioannides[b], Daniele Dini[a,*]

[a] *Tribology Group, Department of Mechanical Engineering, Imperial College London, South Kensington Campus, Exhibition Road, London SW7 2AZ, UK*

[b] SKF Research & Development Company B.V., *Engineering & Research Centre, Kelvinbaan 16, 3439 MT Nieuwegein, The Netherlands*

*Corresponding author: Tel.: +4402075947242; Fax: +4402075947023; Email address: d.dini@imperial.ac.uk

Abstract

This article presents a novel approach for modelling rolling contact fatigue cracks in the presence of lubricants. The proposed formulation captures the interaction between fluid pressure and solid deflections both at the contact interface and along the crack faces using a fully coupled finite volume/boundary element solver. This enables shedding light on the mechanisms which govern crack propagation in various loading conditions and geometrical configurations. It is shown that by linking the fluid behaviour and the elastic deflections within the crack to the film formed at the contact interface it is possible to overcome one of the main limitations of classical models available in the literature, which consists in having to prescribe pressure and/or pressure gradient at the crack mouth during the each loading cycle. The application of linear elastic fracture mechanics principles for the determination of crack stress intensity factors suggests that the results obtained using the approach developed by the authors produce a more realistic characterisation of the crack tip behaviour and it is capable of producing an improved estimate of crack propagation rates. Implications of these findings for the development of rolling contact fatigue lifing tools and potential extensions of the technique are also discussed.

Keywords: *Rolling Contact Fatigue; Hydrodynamic Lubrication; Lubricated cracks; Fluid/Solid coupled interactions; Finite Volume method; Distributed Dislocations technique.*

Nomenclature

a = crack lenght (m)	**Greek symbols**
A = area (m^2)	α = dimensionless flow factor
b = contact width (m)	β = dimensionless flow factor ($\alpha/2$)
b_x, b_y = Burgers vector components	δ, φ, ζ = complex potentials
B = dimensionless contact width	ϕ = bounded part of the dislocation densities
B_x, B_y = dislocation densities	γ = sampling frequency
c, d = position of dislocation	η = viscosity (kg/ms)
e = displacement (m)	κ = Kosolov's constant
f = friction coefficient	λ = finite volume source term
g =	μ = shear modulus (N/m^2)
G = influence function	θ = angle of incline of the crack (°)
h = film thickness (m)	σ = stress (N/m^2)
H = Heaviside step function	ψ = finite volume source terms

k = gradient of convergent wedge

K = dislocation kernels

KI, KII = stress intensity factors (N/m$^{3/2}$)

L = Solid – Liquid Loop iteration step

N = normal traction on crack face (N/m^2)

M = number of cells in finite volume mesh

n = number of points in quadrature scheme

p = pressure (Pa)

P = pressure (Pa)

q = volumetric flux (m^3/s)

R = Radius of the roller

S = shear traction on crack face (N/m^2)

t = time (s)

u = integration points

U = lateral velocity (m/s)

U_s = rolling velocity (m/s)

v = collocation points

V = volume (m^3)

W = normal load (N/m)

x, y = global co-ordinate system axes

$\hat{x}$,$\hat{y}$ = rotated co-ordinate system axes

z = complex variable for the complex potentials

Abbreviations

CFV = Coupled Finite Volume

ESM = Elastic Solver Mesh

FE = Finite Element

FPM = Fluid Pressure Model

FSM = Fluid Solver Mesh

FV = Finite Volume

FVM = Finite Volume Method

LEFM = Linear Elastic Fracture Mechanics

MP = Material Properties

RCF = Rolling Contact Fatigue

SIF = Stress Intensity Factor

SOF = Squeeze Oil Film

SOR = Successive Over Relaxation

TPM = Tapered Pressure Model

ξ = finite volume coefficient

ω = dislocation density weight function

Γ = bulk modulus (N/m^2)

Subscripts and superscripts

0 = condition at the boundaries

c = cracked

C = for the crack film

dd = due to the dislocation densities

f = due to the action of the fluid

in, out = for flux in or out of the system

ii, jj, ij = for xx, yy or xy components

i, k = for the discretised values of u and v

m = finite volume cell number

max = maximum

mouth = crack mouth

N = for the normal stress

op = open

S = for the shear stress

tip = crack tip

tr = for a triangular stress distribution

T = total deflections

τ = time step index

u = un-cracked

^ = for the rotated co-ordinate system

* = dimensionless variable

1. Introduction

Rolling contact fatigue (RCF) affects the life of gears, rolling-element bearings, industrial rollers in the steel-making process, railway wheels and lines, and a number of other important machine elements. It can occur in both lubricated and dry contacts, where a fluid may be intermittently present (for example moisture on railway wheels and lines). Because of the range of conditions that lead to rolling contact fatigue many investigations into the damage and failure mechanisms have been conducted (e.g. [1-6]). Cracks can nucleate both at the contact surface and subsurface, generally in the presence of defects [7]. Also in the latter case, they can grow under repeated contact loading to produce surface-breaking cracks, which, clear symptom of RCF, have been the focus of much of the existing research. Generally inclined [3, 8] and open toward the surface, exposed to the action of liquid present in the surrounding environment (water, oil etc.), they have been observed to lead to pitting [4, 6] and catastrophic failure [9]. Experimental and theoretical work suggests that they propagate by a fatigue mechanism generated by cyclic stresses from repeated rolling and sliding.

There has been speculation as to whether the presence of a fluid is a necessary or a significant part of the failure process. This has led to some diversity in the literature. Authors have presented many different hypotheses aimed at defining how the presence and nature of a lubricant could directly interact with a developing crack and how it may affect the fatigue life of a rolling element. Although there is a difference of opinion on the process, the literature does converge upon one common conclusion: that lubricant plays a role in the propagation of rolling contact fatigue cracks.

Experimental and theoretical work carried out in the past three decades [2, 10-15] has led to the following theories on the role that the fluid may play in fatigue crack growth by: (i) reducing the friction between the crack faces [11] (“friction reduction” shear mechanism); (ii) applying direct pressure on the crack faces as fluid flows into the crack and becomes pressurized under the contact loading [3] (“hydraulic pressure” tensile mechanism); (iii) “fluid entrapment effect” [8] which causes a hydrostatic pressure build up at the crack tip (combined shear and tensile mechanism). Together with these three quasi-static mechanisms, a fourth mechanism has also been proposed, which is based on “the squeeze fluid layer” and therefore considers some of the transient effects which take place inside the cracks [1].

Among the existing models, both the “fluid entrapment” and the “squeeze fluid layer” theories are based on a grounded physical understanding of the phenomenon under investigation. However, no attempt has yet been successful in fully characterising the transient interaction between the pressurized fluid and the solid material. This paper aims to shed light on the liquid/solid interaction in RCF via the development of a new approach for the analysis of lubricated RCF cracks. This will, in turn, lead to an improved understanding of the mechanisms that govern the evolution of surface-breaking cracks into pits, micro-pits and branched cracks. The authors have devised a methodology to fully couple a hydrodynamic model, which accounts for the presence and the behaviour of the fluid both in the contact and within the crack, with advanced linear elastic fracture mechanics tools, which account for the response of the cracked solid body.

2. Strategy and Formulation

The physical problem considered in this paper is shown in Fig. 1(a). The model is a simplified roller element bearing in contact with a cracked lubricated raceway (or equivalently a wheel in contact with a cracked railway), where the components in contact are of similar materials. It has been approximated by considering a cracked semi-infinite, elastic body loaded by a cylindrical roller. The roller is supported by a pressurised lubricant film in the hydrodynamic lubrication regime.

The cylindrical roller is further simplified using a flat convergent surface (see Fig. 1(b)) in order to reduce the complexity of the fluid response at the contact interface as we are mainly interested in the fluid flow and its interaction with the solid within the crack. In first approximation, this corresponds to neglecting the divergent section of the roller, where the fluid experiences cavitation (e.g. see Sommerfeld solution [16]), while still being able to generate the fluid support given by the pressure build-up at the contact interface. The length of hydrodynamic wedge B, the convergence gradient k, and the load W, are imposed and the minimum film thickness h_{in}, is calculated from hydrodynamic theory. The convergence gradient of the wedge is chosen to generate a pressure profile similar to that of the half-Sommerfeld solution for a roller characterised by a radius R in hydrodynamic lubrication regime and generating a minimum film thickness corresponding to h_{out}. The equivalence between the two problems is achieved by matching the load supported by the fluid film, W (see Section 3).

Figure 1

The following simplifying assumptions are made in formulating the problem:

1. The solid model obeys linear elasticity;
2. The radius of curvature of the roller is much larger than the contact region;
3. The crack surface and outer surfaces are perfectly smooth;
4. The deformation of the surface of the cracked body do not affect the hydrodynamic solution at the roller/half-plane interface;
5. The fluid domain is fully flooded;
6. The lubricant is iso-viscous and Newtonian.

It is important to understand the limitations inherent in these assumptions. Assumptions (1) and (2) are justified in the case of most engineering applications such as wheel rail contacts and bearings in which the displacements remain elastic except for a small zone at the crack tip and the material stiffness is high which leads to small contact patches and concentrated high pressures. Assumption (3) is valid in most cases although it should be noted that the crack faces in RCF cracks are not smooth. Assumption (4) is valid only in the case of a lightly loaded contact; this limitation will be addressed in future studies. Assumption (5) encompasses two sub-assumptions: (a) that the contact at the surface is working in the fully flooded regime (which is likely to be true in rolling element bearings but unlikely in wet wheel rail contacts) (b) that the crack is totally filled with fluid prior to entering the contact. There is some experimental evidence for this latter assumption in wheel rail contacts [17] although no data is available for oil lubricated rolling element bearings. Assumption (6) is not true for bearings lubricated with mineral oils; however it is valid for wheel rail contacts where the “lubricant” is water. This will be addressed in future studies.

At an incremental time-step, *t*, two independent algorithms, namely a fluid solver based on a finite volume representation of the Reynolds' equation [18] and an elastic solid solver based on the distributed dislocation technique [19], are coupled at the liquid/solid interface. A schematic of the strategy adopted for the two solvers is shown in Fig. 2 and a flow chart describing a step-by-step implementation of the coupled algorithms is reported in Appendix A. The interaction between the two algorithms is performed using an iterative scheme that, at each time step, alternates between the solvers until the pressure of the lubricant inside the crack and the resulting displacement of the crack faces converge within a specified accuracy range.

Figure 2

2.1. Fluid Formulation

The flow of the lubricant in the crack and in the contact are modelled using the thin film Reynolds equation [20], Eq. (1). The problem is assumed to be isothermal in nature and the lubricant is iso-viscous and Newtonian in behaviour. The formulation of the problem is essentially an extension of the squeeze film model proposed by Bogdánski [1] to include the surface film. If the fluid domain is divided into two parts, namely the surface film and the crack film (see Fig. 2), the problem is generally described, in dimensionless form[1], by:

$$\alpha \frac{\partial h^*}{\partial t^*} + \nabla\left(-h^{*3}\nabla p^* + \beta h^* + q^*_c\right) = 0, \qquad (1)$$

where $\alpha = \frac{12a^2 U_s \eta}{W h_0^{\,2}}$, $\beta = \frac{\alpha}{2}$ and q^*_c are additional sources of flow within the domains. In particular, q_c is the term which is used to couple the solutions of the two regions at the crack mouth (see §2.1.1). The boundary conditions to be considered for the surface film are atmospheric pressure (p_0) at both the inlet and outlet boundaries; here the film thickness is imposed at all points and takes the form of a convergent surface defined by the gradient of the convergence wedge, *k*. The minimum surface film thickness, h_0, is calculated from hydrodynamic lubrication theory as:

$$h_0 = \sqrt{\frac{-6U_s \eta B^2 k_0}{W}} \qquad \text{and} \qquad k_0 = \frac{1}{k^2}\left(-log[k+1] + \frac{2k}{k+2}\right) \qquad (2)$$

The crack film boundary conditions are zero pressure gradient at the crack tip (*i.e.* no flux) and a pressure gradient driven by the flux in and out of the crack at the interacting boundary at the crack mouth. The film thickness within the crack is the combination of the initial crack film thickness, which is set to be equal to the plastic radius at the crack tip, h_{c0}, and the instantaneous total crack deflection, $e^T_{\hat{y}}(\hat{x})$. It is argued that the crack faces, in the absence of any remote load applied to the cracked body, are separated by a

[1] It should be noted here that all the variables carrying the superscript * have been expressed in dimensionless form: the crack length, *a*, *Wa*, and *a/U* have been respectively chosen as unit of length [L], unit of force [F], and unit of time [T]. All these quantities can be therefore re-written in their dimensional form using simple transformations, e.g. $B=B^*a$, $p=(p^*W)/a$, etc…

distance which corresponds to the residual plastic deformation at the crack tip. This can be calculated using linear elastic fracture mechanics (LEFM) models (e.g. Dugdale-type models [21]). Example calculations for the geometry, lubricants and loading conditions explored in this paper (see Table 1) show that the plastic crack tip opening displacement obtained considering the evolution of the mode I stress intensity factors during the loading cycle and using the Dugdale model correspond to values of h_{c0} in the 100 to 200 nm range. The value of h_{c0} used in the analyses presented below is therefore chosen in such range and it is, at least in first approximation, deemed as representative of the operating conditions studied in this article. A more accurate analysis would require a more detailed calculation of the evolution of the plastic field ahead of the crack tip but this is outside the scope of the present contribution.

The fluid domain is mass conserving; this implies that the flow of the lubricant into the system is equal to the flow of lubricant out of the system combined with the source term between the surface film and the crack film ($q_{in} = q_{out} + q_c$). The crack can draw lubricant from the surface film (positive flux) as it opens and squeeze lubricant into the surface film as it closes (negative flux). The interaction between the films gives a coupled response from the fluid, with each film affecting the fluid flow and the pressure distribution in the other.

An analytical solution of the second order differential equation (1) is not trivial and numerical techniques are usually sought to tackle the problem. A finite volume method (FVM), similar to that of Arghir [18], is used here to discretise Eq.1, whereby the fluid domain is divided into a series of control volumes or cells. The governing equation is then integrated over each individual control volume which results in the equation being reduced to the sum of the fluxes acting at each cell interface. The discretisation is conservative and independent of the numerical scheme used for interpolating the face fluxes. Figure 3 shows an arbitrary fluid domain which is discretised into M cells using a structured grid with uniform spacing, Δy^*. The variables are stored at the cell centres.

Figure 3

Integration of Eq. (1) over each individual volume produced by the FVM discretisation gives:

$$\int \alpha \frac{\partial h^*}{\partial t^*} dV^* + \int \beta \frac{\partial h^*}{\partial y^*} dV^* + \int \frac{\partial q_c^*}{\partial y^*} dV^* - \int \frac{\partial}{\partial y^*}\left(h^* \frac{\partial p^*}{\partial y^*} \right) dV^* = 0, \tag{3}$$

which in discretised form reads:

$$\alpha \left[\frac{\left(h^* V^*\right)^{\tau} - \left(h^* V^*\right)^{\tau-1}}{\Delta t^*} \right] + \beta \begin{bmatrix} \left(A^*_{m+0.5}\right) h^*_{m+0.5} \\ -\left(A^*_{m-0.5}\right) h^*_{m-0.5} \end{bmatrix}^{\tau} + \left[q_c^* V^* \right]^{\tau} - \begin{bmatrix} \left(h^{*3} \frac{A^*}{\Delta y^*} \right)_{m+0.5} \left(p^*_{m+1} - p^*_m \right) \\ -\left(h^{*3} \frac{A^*}{\Delta y^*} \right)_{m-0.5} \left(p^*_m - p^*_{m-1} \right) \end{bmatrix}^{\tau} = 0, \tag{4}$$

where τ-*1* denotes the previous time-step and τ denotes the current time-step. This can be written in the tri-diagonal form:

$$\xi^*_m p^*_m - \xi^*_{m-1} p^*_{m-1} - \xi^*_{m+1} p^*_{m+1} = \psi^*_m + \psi^*_q, \tag{5}$$

where

$$\xi^*_m = \xi^*_{m-1} + \xi^*_{m+1}$$

$$\xi^*_{m-1} = \left(h^{*3} \frac{A^*}{\Delta y^*} \right)_{m-0.5}$$

$$\xi^*_{m+1} = \left(h^{*3} \frac{A^*}{\Delta y^*} \right)_{m+0.5}$$

$$\psi^*_q = -V^* q^*_c \tag{6}$$

and

$$\psi^*_m = -\left(\beta \left(\left(A^* h^* \right)_{m+0.5} - \left(A^* h^* \right)_{m-0.5} \right)^\tau + \frac{\alpha}{\Delta t^*} \left(\left(h^* V^* \right)^\tau - \left(h^* V^* \right)^{\tau-1} \right) \right). \tag{7}$$

It should be noted that in Eq. (6) we have introduced a source term to allow coupling with additional flows at the boundaries of the cells, ψ_q. This will be used to couple the fluid solver at the crack mouth.

The discretised expression in Eq. (5) can then be evaluated using any suitable method for tri-diagonal systems of equations. In this study the Successive Over Relaxation (SOR) algorithm was implemented to solve the system of equations resulting from the discretisation of the fluid domain.

The numerical procedure described above requires special care when the coupling the two fluid domains and crack closure are considered. These specific features of the fluid solver are discussed in the following subsection.

2.1.1. Fluid domain coupling

As mentioned above, although the FVM formulation used is the same for the entire fluid domain, the solver is split into two separate parts, one dealing with the film formed between the slider and the half-plane surface, and the other with the fluid film inside the crack. They are coupled using a term characterising the flow exchange between the two films. The corresponding volumetric flux term is characterised by the pressure gradient and the film thickness at the crack mouth and is given by:

$$q^*_c = -h^{*3}_{mouth} \frac{dp^*_{mouth}}{d\hat{x}^*}. \tag{8}$$

This term therefore constitutes a boundary condition for the solution of the crack film (it provides the link between the pressure gradient and the flux at the boundary) and an additional term in flux for the FV element in the surface film which is located at the crack mouth. The solution is iterated until the incremental change in the sum of the squares of the elemental residuals of pressure solution for each iteration between the surface and crack film has dropped below 10^{-5}, i.e. the total residual has dropped below 0.001%.

2.1.2. *Crack closure*

If the crack closes and fluid becomes entrapped within the crack, the fluid pressure solution is no longer coupled, and the flux between the two films (q_c) tends to zero. The surface pressure can then simply be evaluated using the analytical solution for the convergent wedge [20] and the entrapped fluid can be evaluated using the principle of compressibility by taking a constant value of bulk modulus (Γ) where: $\Gamma^* = -V^* \frac{\partial p^*}{\partial V^*}$.

2.2. Solid Formulation

2.2.1. *Problem description*

The solid solver evaluates the effect of fluid pressure acting on the cracked body. Based on linear elastic theory it is expressed as a two-dimensional half-plane whilst invoking the assumptions of plane strain. The methodology is derived from Bueckner's principle (Bueckner 1958) which is based on the superposition of stresses [19]. The influence of plasticity at the crack tip on the solution is assumed to be negligible so the problem can be solved with relative accuracy using liner elastic theory [22].

The stress and displacements resulting from the imposed external load are considered to satisfy equilibrium and compatibility when the effect of the presence of a crack is considered. This divides the solution into two separate problems, which can be superimposed; zero shear tractions and normal tractions equal and opposite to the fluid pressure acting at the crack faces must be enforced to ensure equilibrium (see Fig. 2). The first sub-set of solutions required is the state of stress in an un-cracked body subject to external loads (problem I in Fig. 2). The second problem is that corresponding to glide and climb dislocations, of unknown magnitude, deployed along the crack path (problem II in Fig. 2).

Considering the two problems separately, from the superposition principle we can write that the resultant state of stress in the cracked body is equal to the sum of the contributions from these three problems. This can be expressed mathematically as:

$$\sigma_{ij}^{c}(x,y) = \sigma_{ij}^{u}(x,y) + \sigma_{ij}^{dd}(x,y), \tag{9}$$

where the superscripts *c, u,* and *dd* refer to the cracked, un-cracked, and dislocation densities contributions respectively.

This is true, provided that the boundary conditions at the crack faces and at the remote boundaries (at "infinity") are satisfied. For a surface breaking slant crack, considering the rotated coordinate system ($\hat{x},\hat{y}$) and denoting the normal and shear stresses along the crack faces $N(\hat{x})$ and $S(\hat{x})$ respectively [19] and the value of the fluid pressure along the crack face by $p^f(\hat{x},0)$, the boundary conditions can be written as:

$$\begin{aligned} N(\hat{x}) &= \sigma_{\hat{x}\hat{x}}^{u}(\hat{x},0) + \sigma_{\hat{x}\hat{x}}^{dd}(\hat{x},0) = -p^f(\hat{x}) \\ S(\hat{x}) &= \sigma_{\hat{x}\hat{y}}^{u}(\hat{x},0) + \sigma_{\hat{x}\hat{y}}^{dd}(\hat{x},0) = 0 \end{aligned} \qquad \forall a_{op} < \hat{x} < a \tag{10a}$$

$$N(\hat{x}) = \sigma^{u}_{\hat{x}\hat{x}}(\hat{x},0) + p^{f}(\hat{x},0) + \sigma^{dd}_{\hat{x}\hat{x}}(\hat{x},0) < 0; \qquad g(\hat{x}) = 0$$
$$S(\hat{x}) + fH(\hat{x} - a_{op})N(\hat{x}) = \sigma^{u}_{\hat{x}\hat{y}}(\hat{x},0) + \sigma^{dd}_{\hat{x}\hat{y}}(\hat{x},0) + fH(\hat{x} - a_{op})N(\hat{x}) = 0 \qquad \forall 0 < \hat{x} < a, \tag{10b}$$

where $\hat{x} = x\cos\theta$, $\hat{y} = x\sin\theta$, a is the crack closure length, a_{op} is the open portion of the crack, $g(\hat{x})$ is the surface gap function (hence equal to zero when the crack is closed) and H is the Heaviside step function, $H(\hat{x} - a_{op}) = 1$ when $\hat{x} < a_{op}$ and zero when $\hat{x} > a_{op}$.

Furthermore, due to the very low values of friction used here to reproduce the presence of fluid between the crack faces, the assumption is made that when the crack is partially closed stick does not occur at any point within the crack interface. The presence of stick and slip transition along the crack could however be easily captured following a more general scheme which accounts for stick-slip transitions at the contact interface [19]. Eqs. (10a,b) can be combined to give:

$$N(\hat{x}) = -p^{f}(\hat{x}) \qquad \forall a_{op} < \hat{x} < a$$
$$S(\hat{x}) + fH(\hat{x} - a_{op})N(\hat{x}) = 0 \qquad \forall 0 < \hat{x} < a_{op}. \tag{11}$$

The combined boundary conditions above require that when $a_{op} > 0$ the two stress fields, normal and shear, be evaluated over different intervals. In the closed section of the crack the normal stress field is not altered by the presence of the crack and no discontinuity in the stress field is observed, while the shear is still evaluated over the full crack length.

Once the problem has been formulated, our aim is to find the unknown distribution of dislocations which satisfies the boundary conditions given by Eq. (11).

2.2.2. Solving blocks

The analytical and semi-analytical formulations used to derive the stress and displacement fields within the half-plane for problems I and II will first be individually described. The effects of the loading at the bearing surface (I) can be evaluated using Muskelishvili's potential theorem: in particular, here the contribution of the external load can be evaluated using the solution for triangular influence functions applied to the surface of the half-plane [23]. The stress and displacement fields created by the introduction of the distributed dislocations along the crack faces (II) can then be computed using the technique described *e.g.* in Refs. [19, 24, 25].

Problem I

The stress field induced by the load exerted by the rolling element via the surface film on the un-cracked half-plane can be found by applying Muskelishvili's potential theorem for a surface loaded half-plane using a piece-wise linear triangular discretisation of the pressure along the contact length, B (see Fig. 2 and Ref. [26]). The stress components can be expressed in terms of the complex potential $\varphi(z)$ and its derivatives. The formulation allows the problem to be reduced to a Riemann-Hilbert problem in complex variable theory, where the coordinate system is expressed in the form:

$$z = y - ix, \tag{12}$$

where $.i = \sqrt{-1}$. The relationship between the potential and the stress components is therefore expressed as:

$$\sigma_{xx}^{u,tr} + \sigma_{yy}^{u,tr} = 2[\varphi_{tr}(z) + \overline{\varphi_{tr}(z)}] \tag{13a}$$

$$2\sigma_{xx}^{u,tr} + 2\sigma_{yy}^{u,tr} - 2.i\sigma_{xy}^{u,tr} = 2[(\bar{z} - z)\varphi_{tr}'(z) - \overline{\varphi_{tr}}(z) - \varphi_{tr}(z)] \tag{13b}$$

where $\varphi'(z)$, $\overline{\varphi(z)}$, and $\bar{\varphi}(z)$ are the first derivative, the conjugate function and the conjugate function in the conjugate variable of $\varphi(z)$ respectively. The potential function for a triangular load element of magnitude *p(y)* and centred at (*x=0*, *y=0*) is adopted here:

$$\varphi_{tr}(z) = \frac{p(y)}{2\pi.i}\left(1 - \frac{z}{b_{tr}}\right)\ln\left(\frac{z - b_{tr}}{b_{tr}}\right) - \left(1 + \frac{z}{b_{tr}}\right)\ln\left(\frac{z + b_{tr}}{z}\right), \tag{14}$$

where b_{tr} is the width of each individual triangle. The displacement field induced by each individual triangle at a point within the half-plane (e_x, e_y) can also be found using:

$$2\mu\left(e_x^{tr} + .ie_y^{tr}\right) = \kappa\delta_{tr}(z) - z\overline{\delta_{tr}'(z)} - \overline{\zeta_{tr}(z)}, \tag{15}$$

where $\delta_{tr}'(z) = \varphi_{tr}(z)$ and $\zeta_{tr}'(z) = -z\varphi_{tr}'(z) - \overline{\varphi_{tr}}(z) - \varphi_{tr}(z)$. This implies that only the displacement derivatives can be found in closed form by integrating the above potential functions. The absolute displacements are therefore approximated by the relative displacements with respect to a datum point very remote from the surface. The stress and the displacement fields within the un-cracked body can therefore be calculated by superimposing the contributions of each individual triangle of tractions. Note that the Mohr's circle transformation is applied to the stresses to give the stress field relative to the rotated crack co-ordinate system ($\hat{x}$,$\hat{y}$).

Figure 4

Problem II

Represented by a line of discontinuity in the stress field of a half-plane, the presence of the crack is simulated using strain nuclei (dislocations) of unknown densities along the crack path. This method, which goes under the name of distributed dislocation technique, is based on the principles of linear elastic fracture mechanics and is well documented in the literature [19, 25]. Therefore, only a brief description of the formulation for the specific application of the technique to a surface-breaking slant crack is reported here.

The stresses induced at a point (*x, y*) due to a single dislocation positioned at (*c, d*) can be found from the Airy stress function, which is a solution to the bi-harmonic equation, as [23]:

$$\sigma_{ij}^{dd}(x,y) = \frac{2\mu}{\pi(\kappa+1)}\left(b_x G_{xij}(x,y,c,d) + b_y G_{yij}(x,y,c,d)\right) \tag{16}$$

where the, b_x and b_y, are the 'glide' and 'climb' components of the Burgers vector representing the strain nucleus, and G_{xij} and G_{yij} are known influence functions reported in Ref. [19], with two of them containing a simple Cauchy kernel and the other two being bounded.

In order to simplify the mathematical formulation of the problem, it is customary to solve with respect to a local coordinate system rotated to the angle of incline of the crack (θ). The Burgers vector components can be expressed in the rotated coordinate system by multiplying using the rotation matrix:

$$\begin{pmatrix} b_x \\ b_y \end{pmatrix} = \begin{pmatrix} \cos\theta & \sin\theta \\ -\sin\theta & \cos\theta \end{pmatrix} \begin{pmatrix} b_{\hat{x}} \\ b_{\hat{y}} \end{pmatrix}. \tag{17}$$

By substituting Eq. (17) back into Eq. (16) and applying Mohr's circle transformation, the normal and shear components of the stress tensor due to one dislocation can be written in the rotated coordinate system in terms of the rotated Burgers vector as:

$$\sigma^{dd}_{\hat{y}\hat{y}}(\hat{x},\hat{y}) = \frac{2\mu}{\pi(\kappa+1)}\left(b_{\hat{x}}K^N_{\hat{x}}\left(\hat{x},\hat{y},\hat{c},\hat{d}\right) + b_{\hat{y}}K^N_{\hat{y}}\left(\hat{x},\hat{y},\hat{c},\hat{d}\right)\right) \tag{18a}$$

$$\sigma^{dd}_{\hat{x}\hat{y}}(\hat{x},\hat{y}) = \frac{2\mu}{\pi(\kappa+1)}\left(b_{\hat{x}}K^S_{\hat{x}}\left(\hat{x},\hat{y},\hat{c},\hat{d}\right) + b_{\hat{y}}K^S_{\hat{y}}\left(\hat{x},\hat{y},\hat{c},\hat{d}\right)\right), \tag{18b}$$

where $\hat{x} = \cos\theta(x)$, $\hat{y} = \sin\theta(x)$, $\hat{c} = \cos\theta(c)$, and $\hat{d} = \sin\theta(c)$, and $K^N_{\hat{x}}, K^N_{\hat{y}}, K^S_{\hat{x}}, K^S_{\hat{y}}$ are the transformed kernels. If we now consider the effect of a continuous distribution of infinitesimal burgers vectors along the crack line, whose densities are

$$B_{\hat{x}}\left(\hat{c}\right) = \frac{db_{\hat{x}}(\hat{c})}{d\hat{c}};\ B_{\hat{y}}\left(\hat{c}\right) = \frac{db_{\hat{y}}(\hat{c})}{d\hat{c}}, \tag{19}$$

the tractions along the crack faces in the rotated coordinate system are given by:

$$\begin{aligned} \sigma^{dd}_{\hat{y}\hat{y}}(\hat{x}) &= \frac{2\mu}{\pi(\kappa+1)}\left(\int_0^a B_{\hat{x}}(\hat{c})K^N_{\hat{x}}(\hat{x},\hat{c})d\hat{c} + \int_{a_{op}}^a B_{\hat{y}}(\hat{c})K^N_{\hat{y}}(\hat{x},\hat{c})d\hat{c}\right) \\ \sigma^{dd}_{\hat{x}\hat{y}}(\hat{x}) &= \frac{2\mu}{\pi(\kappa+1)}\left(\int_0^a B_{\hat{x}}(\hat{c})K^S_{\hat{x}}(\hat{x},\hat{c})d\hat{c} + \int_{a_{op}}^a B_{\hat{y}}(\hat{c})K^S_{\hat{y}}(\hat{x},\hat{c})d\hat{c}\right) \end{aligned} \tag{20}$$

It should be noted here that in case the crack is fully opened both sets of dislocations are distributed along the entire length of the crack, $0 < \hat{x} < a$; if, instead, part of the crack is closed the climb dislocations are only distributed along the opened portion of the crack, $a_{op} < \hat{x} < a$. A further characteristic of the solution is that the crack opening, $e^{dd}_{\hat{y}}(\hat{x})$, and the relative tangential displacement along the crack faces, $e^{dd}_{\hat{x}}(\hat{x})$, at any location within the opened portion of the crack can always be directly obtained by integrating the climb dislocation density between the crack tip and the location of interest, $\hat{x}$:

$$\begin{aligned} B_{\hat{y}}\left(\hat{c}\right) = -\frac{de^{dd}_{\hat{y}}(\hat{c})}{d\hat{c}} &\Rightarrow e^{dd}_{\hat{y}}(\hat{x}) = -\int_a^{\hat{x}} B_{\hat{y}}\left(\hat{c}\right)d\hat{c} \\ B_{\hat{x}}\left(\hat{c}\right) = -\frac{de^{dd}_{\hat{x}}(\hat{c})}{d\hat{c}} &\Rightarrow e^{dd}_{\hat{x}}(\hat{x}) = -\int_a^{\hat{x}} B_{\hat{x}}\left(\hat{c}\right)d\hat{c}. \end{aligned} \tag{21}$$

2.2.3. Solution

Once the three stress fields corresponding to the three solving blocks of the solid solver have been derived, Eq. (11) becomes:

$$
\begin{aligned}
&N(\hat{x}) = \sigma^{u}_{\hat{y}\hat{y}}(\hat{x},0) + \frac{2\mu}{\pi(\kappa+1)}\left(\int_0^a B_{\hat{x}}(\hat{c})K^{N}_{\hat{x}}\left(\hat{x},\hat{c}\right)d\hat{c} + \int_{a_{op}}^a B_{\hat{y}}(\hat{c})K^{N}_{\hat{y}}\left(\hat{x},\hat{c}\right)d\hat{c}\right) = -p^{f}(\hat{x}), \qquad \forall a_{op} < \hat{x} < a \\
&S(\hat{x}) + fH(\hat{x}-a_{op})N(\hat{x}) = \\
&= \sigma^{u}_{\hat{x}\hat{y}}(\hat{x},0) + \frac{2\mu}{\pi(\kappa+1)}\left(\int_0^a B_{\hat{x}}(\hat{c})K^{S}_{\hat{x}}\left(\hat{x},\hat{c}\right)d\hat{c} + \int_{a_{op}}^a B_{\hat{y}}(\hat{c})K^{S}_{\hat{y}}\left(\hat{x},\hat{c}\right)d\hat{c}\right) fH(\hat{x}-a_{op})N(\hat{x}) = 0, \quad \forall 0 < \hat{x} < a.
\end{aligned}
\tag{22}
$$

The presence of Cauchy kernels, which become singular as $\hat{x}$ tends to $\hat{c}$, implies that Eq. (22) cannot be solved in closed form. Therefore, a robust quadrature scheme is required to obtain an approximate solution. The interval of integration is first normalised by:

$$
\begin{aligned}
&v = \frac{2\hat{x}}{a} - 1, \qquad 0 < \hat{x} < a \\
&u = \frac{2\hat{c}}{a} - 1, \qquad 0 < \hat{c} < a
\end{aligned}
\tag{23}
$$

$$
\begin{aligned}
&\bar{v} = \frac{2\left(\hat{x}-a_{op}\right)}{a-a_{op}} - 1, \qquad a_{op} < \hat{x} < a \\
&\bar{u} = \frac{2\left(\hat{c}-a_{op}\right)}{a-a_{op}} - 1, \qquad a_{op} < \hat{c} < a
\end{aligned}
\tag{24}
$$

This gives the integral equations in normalised form as:

$$
\begin{aligned}
&\sigma^{u}_{\hat{y}\hat{y}}(\bar{v}) + \frac{2\mu}{\pi(\kappa+1)}\left(\int_{-1}^1 B_{\hat{x}}(u)K^{N}_{\hat{x}}\left(\bar{v},u\right)du + \int_{-1}^1 B_{\hat{y}}(\bar{u})K^{N}_{\hat{y}}\left(\bar{v},\bar{u}\right)d\bar{u}\right) = -p^{f}(\bar{v}), \qquad \forall -1 < \bar{v} < 1 \\
&\sigma^{u}_{\hat{x}\hat{y}}(v) + \frac{2\mu}{\pi(\kappa+1)}\left(\int_{-1}^1 B_{\hat{x}}(u)K^{S}_{\hat{x}}\left(v,u\right)du + \int_{-1}^1 B_{\hat{y}}(\bar{u})K^{S}_{\hat{y}}\left(v,\bar{u}\right)d\bar{u}\right) fH\left(v - \frac{a_{op}}{a}\right)N(v) = 0. \quad \forall -1 < v < 1
\end{aligned}
\tag{25}
$$

To evaluate the singular integrals it is necessary to express the dislocation densities as the product of the bounded functions, $\phi_{\hat{x}}(u)$, $\phi_{\hat{y}}(u)$, and the weight function, $\omega(u)$, $\omega(\bar{u})$ [27], such that:

$$
B_{\hat{x}}\left(u\right) = \phi_{\hat{x}}(u)\omega(u); \;\; B_{\hat{y}}\left(\bar{u}\right) = \phi_{\hat{y}}(\bar{u})\omega(\bar{u}), \tag{26}
$$

where $\phi_{\hat{x}}$ and $\phi_{\hat{y}}$ are two unknown bounded functions and, $\omega(u)$ and $\omega(\bar{u})$ are the regular fundamental functions, which by assuming a bounded (at the crack mouth and at the opening length for glide and climb dislocations respectively) and singular solution for both glide and climb dislocations, are given by $\omega(u) = (1-u)^{-1/2}(1+u)^{1/2}$ and $\omega(\bar{u}) = (1-\bar{u})^{-1/2}(1+\bar{u})^{1/2}$. A Gauss-Jacobi type quadrature is applied to the discrete form of the Eqs. (21): a series of integration (u_k) and collocation (v_i) points are used to discretise the crack length, a, and the opening length, $a_{op} < \hat{x} < a$ using quadrature formulae for bounded and singular Cauchy kernels [19] which produce a set of 2n simultaneous equations with 2n unknowns.

In particular, by discretising the normalised coordinate sets using:

$$u_k,\bar{u}_k = \cos\left(\frac{2k-1}{2n+1}\pi\right); \qquad k = 1,...,n$$
$$v_i,\bar{v}_i = \cos\left(\frac{2i}{2n+1}\pi\right); \qquad i = 1,...,n \tag{27}$$

and combining the integrals with the appropriate weight functions, we obtain:

$$\frac{2\mu}{\pi(\kappa+1)}\sum_{k=1}^{n}\left[\begin{array}{l}\dfrac{2\pi(1+u_k)}{2n+1}\phi_{\hat{x}}(u_k)K_{\hat{x}}^{N}(\bar{v}_i,u_k)+\\ \dfrac{2\pi(1+\bar{u}_k)}{2n+1}\dfrac{a_{op}}{a}\phi_{\hat{y}}(\bar{u}_k)K_{\hat{y}}^{N}(\bar{v}_i,\bar{u}_k)\end{array}\right] = \sigma_{\hat{y}\hat{y}}^{u}(\bar{v}_i) - p^{f}(\bar{v}_i) \qquad i = 1,...,n \tag{28a}$$

$$\frac{2\mu}{\pi(\kappa+1)}\sum_{k=1}^{n}\left[\begin{array}{l}\dfrac{2\pi(1+u_k)}{2n+1}\phi_{\hat{x}}(u_k)\left\{\begin{array}{l}K_{\hat{x}}^{S}(v_i,u_k)+\\ fH\left(v_i-\dfrac{a_{op}}{a}\right)K_{\hat{x}}^{N}(v_i,u_k)\end{array}\right\}\\ +\dfrac{2\pi(1+\bar{u}_k)}{2n+1}\dfrac{a_{op}}{a}\phi_{\hat{y}}(\bar{u}_k)\left\{\begin{array}{l}K_{\hat{y}}^{S}(v_i,\bar{u}_k)+\\ fH\left(v_i-\dfrac{a_{op}}{a}\right)K_{\hat{y}}^{N}(v_i,\bar{u}_k)\end{array}\right\}\end{array}\right] = \left[\begin{array}{l}\sigma_{\hat{x}\hat{y}}^{u}(v_i)+\\ fH\left(v_i-\dfrac{a_{op}}{a}\right)\sigma_{\hat{y}\hat{y}}^{u}(v_i)\end{array}\right]. \quad i = 1,...,n \tag{28b}$$

Eqs. (28) can be easily solved using a standard computer library routine to find the unknown distributions $\phi_{\hat{x}}(u), \phi_{\hat{y}}(u)$. This allows the unknown dislocation densities to be computed and stress and displacement fields induced by the surface loading and the pressurised fluid to be computed everywhere within the solid. Mode I and Mode II stress intensity factors can also be directly evaluated using Krenk's interpolation formulae [28].

2.3. Fluid-Solid Coupling

To capture the transient behaviour of the fluid a time dependent solution is essential. The time step (Δt^*) can be evaluated as a function of the width of the contact, *B**, divided by the number of FV cells, *M*, times the frequency at which the domain is sampled, γ (*e.g.* if every second cell location is used γ = 0.5):

$$\Delta t^* = \frac{B^*}{\gamma M} \tag{29}$$

At each time step, coupling between the solid and the fluid provides the instantaneous value of the film thickness everywhere within the fluid domain. This is captured by an iterative routine that manages the interaction at the solid/fluid interface. The fluid pressures, both at the surface and within the crack, are first calculated using the FVM formulation together with the new boundary condition at the crack mouth derived from the moving load and the crack deflection at the previous load step. These values are then interpolated and applied at the nodes of the solid domain as triangles of tractions (at the half-plane surface). The relative displacement of the crack faces due to the surface loading and the crack film pressure is calculated as the sum of the contributions of the film pressure and the distributed dislocations as:

$$e_{\hat{y}}^{dd}(\hat{x}) + e_{\hat{y}}^{u}(\hat{x}) = e_{\hat{y}}^{T}(\hat{x})$$
$$e_{\hat{x}}^{dd}(\hat{x}) + e_{\hat{x}}^{u}(\hat{x}) = e_{\hat{x}}^{T}(\hat{x}). \quad (30)$$

This is then added to the initial crack film thickness, $h_{c,0}$, which, as mentioned above, can be directly computed considering crack tip plasticity within the LEFM framework. At a specific iteration step, L, the fluid film thickness within the crack is given, in dimensionless form, by:

$$h_C^*(\hat{x},L) = h_{C,0}^* + e_{\hat{y}}^{*T}(\hat{x},L) \quad (31)$$

Every time the film thickness in the crack is changed, the fluid solver is called and the pressures in the FVM solution updated using the modified crack profile. The iterative process is repeated until both fluid pressure and film thickness both inside and outside the crack have reached convergence criteria in the rate of change of film thickness, see appendix A, *i.e.* when:

$$\frac{dh_C^*(\hat{x},L)}{dL} \to 0. \quad (32)$$

Once the solution has converged the next time-step is considered ($t \rightarrow t+\Delta t$) and the position ($Y^*= Y^*+\Delta Y^*$) of the crack relative to the contact centre is updated. The process is repeated until the crack has traversed the loaded area. At each instant, t, the converged solution at the previous time step, $t-1$, is used to initialise the solvers, with the exception of the first step. The first step is initialised using the solution for a dry crack solved outside the contact.

3. Results and Discussion

3.1. Validation of individual solvers and intermediate steps

While it is difficult to find benchmark solutions to validate the fully coupled problem as this is the first instance when a coupled fluid/solid solver is used for RCF cracks in the presence of lubrication, it is important to consider some of the intermediate steps and perform validation of the individual solvers, which correspond to individual blocks of the overall algorithm presented in Appendix A. To this end, the hydrodynamic solution for the linear convergent wedge, the volumetric flux used for the fluid coupling of the two films at the crack mouth and the crack opening due to the fluid pressure acting at the crack faces were considered as the quantities to independently check to verify the validity of the fluid solver, the coupling methodology and the solid solver respectively. Benchmark solutions obtained using either analytical or numerical techniques have been used to assess the accuracy of the proposed algorithms and the suitability of the proposed approach for coupling the fluid and the solid solvers.

In Fig. 5(a) the analytical pressure distribution produced by a linear wedge in the absence of the crack is compared to that produced by the equivalent “half-Sommerfeld” [14] solution for a cylinder on a lubricated plane. Of course, the two solutions do not show perfect agreement as they correspond to different physical problems; however, the similarity between the pressure distributions obtained under the effect of same normal load confirms that using a linear wedge to approximate the physical problem under investigation (see Fig.1) is appropriate for development purposes. The comparison between the FV solution obtained by

the fluid solver implemented by the authors and the analytical solution for a linear convergent bearing is also shown. The two methods compare well, confirming the correctness and the accuracy of the numerical formulation.

Figure 5

As previously stated the coupling between the surface film and the film within the crack is achieved through the use of the flux term evaluated in a cell which bridges the interface between the crack and the surface film. The suitability of this term in representing the flux from the crack to the film or from the film to the crack can be assessed by comparison of this term with the integral change in the crack deflections (*i.e.* the change in the volume of fluid filling the crack). Figure 5(b) shows this comparison; good agreement between the magnitudes of the two measures of flux between the films is demonstrated. It should be noted that positive flux indicates flow into the crack and negative flux corresponds to fluid drawn from the crack. This supports the use of this simple coupling method for application in this problem.

Finally, a measure of the applicability of the current distributed dislocation technique in accurately modelling the presence of pressurised fluid in a cracked solids can be obtained through comparison with converged finite element (FE) solutions (here the FE package ANSYS 11.0 was used). Figure 5(c) shows the results obtained using the two numerical methods for an edge crack in a half-plane with a constant pressure applied along its faces: the deflections at the crack faces, identified here by the crack opening, are again in good agreement with small discrepancies occurring at the crack mouth, mainly due to the difference in the discretisation used for the two techniques.

3.2. Example coupled problems

In this section the case of a rolling contact fatigue crack in a half-plane, inclined at 25° to the surface, traversed by a loaded convergent hydrodynamic bearing is presented as a test case. It serves to outline the method and the framework developed by the authors for analysing lubricated cracks. Three different geometries are considered and compared (see Table 1).

Table 1

Considering case 2, the variation in crack shape and pressure with respect to time, *i.e.* as Y^* varies from -1 to 1, is shown in Fig. 6. In particular, the contours plotted in Fig. 6(a) provide the full history of the crack opening and closure, while Figs. 6(b)-6(d) are “slices” through the contours identified by the letters A to C and provide the deflections experienced at three locations within the crack during the loading cycle. The initial crack opening corresponds to a rapid fluid pressurisation inside the crack and the development of a large positive pressure gradient from crack mouth to crack tip. As a result, the crack begins to draw lubricant from the surface film allowing it to fill. This process continues until the opening reaches a maximum (*i.e.* when the action of the external load balances the effect of the fluid pressurisation), at which point the pressure gradient along the crack length tends to zero. There now exists, although only

instantaneously, a constant pressure distribution similar to that hypothesised when using a hydraulic pressure model [2].

Figure 6 –

Once the crack passes the point of maximum surface pressure, $Y^* > -0.25$, it starts to close and continues to close as Y^* tends to 1. During this phase of the loading cycle, lubricant is squeezed out of the crack and a negative pressure gradient exists from crack tip to crack mouth. As the fluid is squeezed into the surface film, the surface pressure rises; this acts to restrict the flow of lubricant out of the crack. In this way the surface film controls the rate at which the crack closes.

Some comments about the implications that a fully coupled calculation has on the fluid pressure distribution within the crack are appropriate here. Unlike other existing models, the proposed methodology enable to capture the transient evolution of the squeeze term ($\mathrm{d}h(\hat{x})/\mathrm{d}t$). The presence of the crack mouth flux term allows determining the influence of the local surface film pressure on the crack film, therefore overcoming one of the main limitations of uncoupled models. It should be again emphasised that the hypotheses made by such models about the fluid pressure at the crack mouth and the pressure gradient within the crack [1, 4, 12, 29] correspond intrinsically to modify the exchange of flux between the surface film and the crack in an uncontrolled fashion. This results in the possibility for instantaneously infinite flux to occur at the crack mouth during part of the loading cycle. In the proposed coupled model this is not the case; the fluid film on the outer surface and the solid deflections act to regulate the flow at the crack mouth, much like a valve.

If we now focus on the evolution of the pressurised crack shape, Fig. 7 shows the crack deflections, and therefore the crack film shape, at three instants in time immediately before closure. The crack surfaces begin to "arch" towards closure near the crack mouth as the load continues to traverse across the crack, $Y^* > 0.6$. This behaviour is driven primarily by the negative pressure gradient within the crack film. The surface loading at the mouth starts to dominate, prevailing over the internal fluid pressure and as Y^* increases the faces at the crack mouth touch. Then as Y^* continues to increase the section of the crack nearest to the mouth comes into contact.

Figure 7

The closure stops the flow of lubricant between the surface film and the crack film (q_c once again tends to zero) uncoupling the problem and providing a fixed volume of entrapped lubricant. At this point the behaviour of the solution changes and the coupled film FV solution is replaced by an analytical solution for the surface pressure. This is combined with a constant fluid pressure inside the crack resulting directly from the compressibility or bulk modulus of the lubricant. As the load continues to traverse, *i.e.* as Y^* tends from 0.75 towards 1, the entrapped fluid becomes compressed and increasingly pressurised. This pressurized, entrapped fluid maintains a degree of opening at the tip of the crack, restricting the crack from completely closing.

The coupling between the crack film and the surface film can be illustrated and quantified by considering the relationship between the crack mouth displacement, $e_{\dot{y}}^{T}(0)$, the volumetric flux (Fig. 8(a)) and the normalised pressure gradient, Δp^*, in the crack (Fig. 8(b)), where:

$$\Delta p^* = \frac{p_{ctip} - p_{cmouth}}{p_{cmouth}}. \tag{36}$$

Figure 8 shows that, as Y^* varies from *-1* to *1*, there exists a strong relationship between the fluid pressure and the flow of lubricant between surface film and crack film. In the portion of the loading cycle corresponding to positive pressure gradients, *i.e.* when the crack is opening, the lubricant flows into the crack. The magnitude of the flux can be directly correlated to the strength of the positive pressure gradient. The converse is true when the pressure gradient is negative. Furthermore the point at which the solution returns a zero pressure gradient, which is also the point of maximum opening, is directly related to the point of zero flux. This coupling between the crack shape, the pressure and the resulting flow illustrates a strong connection between the solution and the inherent physics of the problem.

Figure 8

Let us now look at the normalised coupling flux term, whose evolution is shown for cases 1-3 in Fig. 9. The results demonstrate that the crack length affects the flow between the surface and the crack film. While the bearing traverses the cracked region, there is a first a positive flux of lubricant, which corresponds to fluid being "pumped" into the crack; this reaches a maximum, when the action of the pressurised liquid is still capable of counteracting the external load, and then starts to decrease until it becomes negative. At this stage fluid starts draining from the crack until closure takes place (or until the load moves away from the cracked portion of the half-pane is closure does not take place): this corresponds to the negative flux peak and to the subsequent reduction of the flux term to zero. For a short crack, $b = 4a$, the transition from positive to negative is reached quickly ($Y^* \approx -0.4$) whilst for the longer crack, $b = a$, the transition comes later ($Y^* \approx 0$). The flow patterns illustrate the effect of the crack length on the cycle of the crack opening and closing. This is because the longer crack has a longer period of opening, which, in turn, leads to the longer crack having a greater period of positive flux because the positive pressure gradient within the crack takes longer to reduce to zero. This intuitively corresponds to the physical behaviour of the system, whereby longer cracks are expected to draw more lubricant from the surface film. Furthermore, the integral of the positive flux is also noticeably larger than the integral of the negative flux which can be attributed to the entrapment of some fluid in the crack when q_c tends to zero at closure.

Figure 9

The Stress intensity factors (SIF) which govern crack propagation are important measures of the criticality of a crack, and its propensity to grow. The relative deviation (ΔK) and the load ratio (R) can be used in a

wide range of models for prediction of crack growth rates, *da/dN*. These include the models first postulated by Paris *et al.* [30] but also a number of more advanced damage accumulation type models [31-34].

Figs. 10a, b shows the normal mode (or mode I) SIF, *KI*, and the shear mode SIF, *KII*, for cases 1-3. Both quantities are normalised using the maximum surface film pressure and the crack length, i.e. $K_I^* = \frac{K_I}{p_{\max}\sqrt{\pi a}}$, where $p_{\max}$ is the maximum pressure at the surface. By comparison of the traces of SIF with those for fluid pressure and opening displacement it is clear that a high degree of coupling exists within the problem. The mode I stress intensity factor with respect to time can be directly related to the severity of the crack opening displacement: the more the crack opens the greater the likelihood of crack growth. Because the pressurized fluid is the factor driving the crack opening, it can be argued that the fluid pressure is directly linked to the severity of crack propagation in the normal mode (*KI*). When the crack experiences partial closure it maintains a degree of opening, therefore *KI* remains greater than zero, but the severity of the damage in this part of the loading cycle strongly depends on the characteristics of the entrapped fluid and can be considered as generally mild.

Figure 10

Focussing now on the mode II stress intensity factor, Fig. 10b shows the evolution of *KII* during the loading cycle. The fluid pressure on the surface dominates the solution; this can be seen from the correlation in shape between *KII* and the fluid pressure. Although less severe than *KI* in absolute value, it can still considerable contribute to crack propagation and kinking. The combined effect of the external loading and of crack opening generates shearing at the crack tip and corresponding relatively large *KII* values. This is strongly affected by the angle of inclination.

From Figures 10(a) and 10(b) it is also clear that the magnitude of the SIF is directly related to the length of the RCF crack. Longer cracks yield higher SIF and, therefore, acceleration in crack growth rate, d*a*/d*N*, is coupled with an increase in crack length. This is an intuitive correlation, because as the crack grows its capacity to open under the action of the internal pressurised fluid increases. The load on the crack faces, i.e. the integral of the pressure along the crack faces, is proportional to crack length. Therefore, as the crack length increases, so does the load applied to the crack faces. This causes and increased tendency of the crack faces to open, which in turn produces a rise in the SIFs and facilitates RCF crack propagation. The amount by which the RCF crack opens during a loading cycle is proportional to the rate at which it will propagate. However, it should be born in mind that the analyses discussed in this paper are under the hypothesis of the crack being fully flooded at the start of the simulation. Obviously, while for short cracks this hypothesis is realistic, for longer cracks it may not be valid as penetration of the fluid within the crack will be a complex function of crack length, bearing speed and viscous property of the fluid (capillary effects might also play a role [10]). The investigation of crack filling is however outside the scope of the present contribution.

Figures 11(a) and 11(b) shows a comparison between the stress intensity factors obtained using the current coupled finite volume (CFV) model, a Squeeze Oil Film (SOF) model [1], an uncoupled fluid

pressure model (FPM), characterised by a constant pressure applied along the crack faces [2, 4, 29], and an uncoupled tapered pressure model (TPM) [4, 12], characterised by a pressure varying linearly along the crack faces. It should be noted that all the models from the literature assume that the behaviour of the fluid within the crack is not directly coupled to the solution of the problem at the contact interface, and therefore the pressure at the crack mouth is arbitrarily defined.

It is immediately clear that the coupled model proposed by the authors gives considerably different results to those produced by any of the models already available in the literature. These differences are twofold. Firstly, the current coupled model captures the physics of the problem and allows following the evolution of the fluid/solid interactions without introducing approximations and/or hypothesis on the evolution of the fluid pressure within the crack. This is achieved by directly computing the effect of the changing crack film shape on the fluid pressure and of the fluid pressure on the fluid flow both inside and outside the crack. This is not possible using other existing models. The uncoupled methodologies in the literature tend to provide an imprecise prediction of the crack displacement history and, as a consequence, of the evolution of the stress intensity factors within the loading cycle [29]. This may lead to significant differences in the predicted crack propagation rates when using a Paris-type crack propagation law [29-32].

Secondly, from Figs. 11(a) and 11(b) it is clear that the range of stress intensity factors (defined as $K_{max} - K_{min}$ for both mode I and mode II) at the crack tip of RCF cracks is strongly affected by the assumptions made at the crack mouth. In the example considered by the authors, the coupled approach produces a reduced range of SIFs as a result of the feedback mechanism created by the interaction between the fluid film in the crack and the fluid film on the surface. Any closure or opening of the crack is driven by the surface pressure. However, when the surface pressure causes a variation in the crack shape; lubricant must be drawn from the surface film or pushed into the surface film; this causes a necessary fluctuation in the surface pressure and reduction in the flux. In this way, a physical feedback loop serves to “damp” the flux between the two sections of the lubricant film and the deflections of the crack face. This limits both the maximum rate of opening and the maximum rate of closure at the crack mouth. As a direct result this gives a reduction in the range of the SIFs; implying a lowering of the predicted mode I and mode II driven crack propagation rates with respect to models which do not employ a fully coupled approach.

Figure 11

4. Conclusions

In summary, the authors have presented a solution to a problem in which a single inclined crack passes through a lubricated rolling line contact. To achieve this, a coupled fluid–solid solver has been developed that uses Linear Elastic Fracture Mechanics (LEFM) to model the solid body and a Finite Volume (FV) formulation of the Reynolds equation to model the lubricant film. This approach predicts differences in both the evolution and the range of the stress intensity factors computed at the crack tip of typical RCF cracks when compared to ‘fluid pressure’ models available in the literature. These differences result primarily from the coupling between the fluid within the crack and the fluid film on the surface, through quantifying the flux at the crack mouth, and serve to demonstrate the importance of considering the surface film. Given similar material characteristics, the results presented in Figs. 11 obtained using the coupled approach developed

by the authors suggest reduced crack propagation rate when a LEFM-based approach is utilised [29-32]. This leads to an increase in predicted component lives, a more realistic outcome with respect to the estimates produced by existing models available in the literature, which are known to over-predict crack propagation rates [29] and only to provide lower bounds on components fatigue life.

To conclude, the methodology proposed by the authors employs a multi-physics solver to capture transient fluid-solid interactions for the accurate description of the physics governing the propagation of RCF cracks in the presence of lubrication. Fluid entrapment and crack closure also feature among the mechanisms which can be dealt with by this approach. The improved prediction of SIFs obtained using the proposed model suggests that further extensions to include the elastic deformation of the contact surfaces, the evolution of cracks shape and dimensions due to the repeated application of the external load, and three-dimensional aspects are likely to produce a powerful RCF lifing tool. These aspects are the subject of ongoing investigations.

Acknowledgements

The authors acknowledge the financial support of the UK Engineering and Physical Sciences Research Council (EP/E034179/1) and SKF Engineering & Research Centre BV. Daniele Dini wishes to thank the Royal Swedish Academy of Engineering Science for the Jacob Wallenberg Foundation grant received in 2007.

5. References

1. Bogdanski, S., *A rolling contact fatigue crack driven by squeeze fluid film.* Fatigue and Fracture of Engineering Materials and Structures, 2002. **25**(11): p. 1061-1071.
2. Bower, A.F., *The influence of crack face friction and trapped fluid on surface initiated rolling contact fatigue cracks.* Transaction of the ASME - Journal of Tribology, 1988. **110**(4): p. 704-11.
3. Kaneta, M.M. and Y.Y. Murakami, *Effects of oil hydraulic pressure on surface crack growth in rolling/sliding contact.* Tribology International, 1987. **20**(4): p. 210-217.
4. Keer, L.M. and M.D. Bryant, *A pitting model for rolling-contact fatigue.* Transactions of the ASME - Journal of Lubrication Technology, 1983. **105**(2): p. 198-205.
5. Olver, A.V., et al., *Direct observations of a micropit in an elastohydrodynamic contact.* Wear, 2004. **256**(1-2): p. 168.
6. Way, S., *Pitting due to rolling contact.* Transactions of the ASME - Journal of Applied Mechanics, 1935. **2**(3): p. -110--114.
7. Keer, L.M., M.D. Bryant, and G.K. Haritos, *Subsurface and surface cracking due to hertzian contact.* Transactions of the ASME - Journal of Lubrication Technology, 1982. **104**(3): p. 347-351.
8. Bower, A.F., *Some Aspects of Plastic Flow, Residual Stress and Fatigue Cracks Due To Rolling and Sliding Contact*, PhD Thesis, School of Engineering, University of Cambridge, 1987.
9. Olver, A.V., *The mechanism of rolling contact fatigue: an update.* Proceedings of the Institution of Mechanical Engineers Part J-Journal of Engineering Tribology, 2005. **219**(J5): p. 313-330.
10. Bogdanski, S., *Liquid-solid interaction at opening in rolling contact fatigue cracks.* Wear, 2005. **258**(7-8): p. 1273-1279.
11. Fajdiga, G., J. Flasker, and S. Glodez, *The influence of different parameters on surface pitting of contacting mechanical elements.* Engineering fracture mechanics, 2004. **71**(4-6): p. 747-758.
12. Kaneta, M., M. Suetsugu, and Y. Murakami, *Mechanism of surface crack-growth in lubricated rolling-sliding spherical contact.* Transactions of the ASME - Journal of Applied Mechanics, 1986. **53**(2): p. 354-360.
13. Murakami, Y., et al., *Experimental and fracture mechanics study of the pit formation mechanism under repeated lubricated rolling-sliding contact: Effects of reversal of rotation and change of the driving roller.* Transactions of the ASME - Journal of Tribology, 1997. **119**(4): p. 788-796.

14. Ringsberg, J.J.W., *Life prediction of rolling contact fatigue crack initiation.* International Journal of Fatigue, 2001. **23**(7): p. 575-586.
15. Akama, M. and T. Mori, *Boundary element analysis of effects of crack face friction and trapped fluid on rolling contact fatigue cracks.* Quarterly Report of RTRI (Railway Technical Research Institute) (Japan), 2005. **46**(4): p. 231-237.
16. Sommerfeld, A., *Zur hydrodynamischen Theorie der Schmiermittelreibung.* Zeitschrift fur Mathematik und Physik, 1904. **40**: p. 97-155.
17. Fletcher, D.I., P. Hyde, and A. Kapoor, *Investigating fluid penetration of rolling contact fatigue cracks in rails using a newly developed full-scale test facility.* Proceedings of the Institution of Mechanical Engineers, Part F: Journal of Rail and Rapid Transit, 2007. **221**(1): p. 35-44.
18. Arghir, M., A. Alsayed, and D. Nicolas, *The finite volume solution of the Reynolds equation of lubrication with film discontinuities.* International Journal of Mechanical Sciences, 2002. **44**(10): p. 2119-2132.
19. Hills, D.A., et al., *Solutions of Cracks Problems - The Distributed Dislocation Technique*. Vol. 1. 1996: Kluwer Academic Publishers.
20. Cameron, A., *Basic Lubrication Theory*. 1971, London: Longman.
21. Wu, S.S.X., Y.Y.W. Mai, and B.B. Cotterell, *A model of fatigue crack growth based on Dugdale model and damage accumulation.* International Journal of Fracture, 1992. **57**(3): p. 253-67.
22. Rice, J.R., *Limitations to the small scale yielding approximation for crack tip plasticity.* Journal of the Mechanics and Physics of Solids, 1974. **22**(1): p. 17-26.
23. Hills, D.A., D. Nowell, and A. Sackfield, *Mechanics of Elastic Contacts*. First ed. 1993: Butterworth-Heinemann Ltd.
24. Hills, D.A. and M. Comninou, *An analysis of fretting fatigue cracks during loading phase.* International Journal of Solids and Structures, 1985. **21**(7): p. 721-30.
25. Nowell, D. and D.A. Hills, *Open cracks at or near free edges.* Journal of Strain Analysis for Engineering Design, 1987. **22**(3): p. 177-85.
26. Bentall, R.H. and K.L. Johnson, *An elastic strip in plane rolling contact.* International Journal of Mechanical Science, 1968. **Vol.10**(1968): p. 637-668.
27. Erdogan, F., G.D. Gupta, and T.S. Cook, *Numerical solution of singular integral equations.* Methods in Analysis and Solutions of Crack Problems, 1973. **1973**: p. 368-425.
28. Krenk, S., *On the use of interpolation polynomial for solutions of singular integral equations.* International Journal of Solids and Structures, 1975. **32**: p. 479-484.
29. Fletcher, D.I., P. Hyde, and A. Kapoor, *Modelling and Full Scale Trials to Investigate Fluid Pressurisation of Rolling Contact Fatigue Cracks.* Wear, 2008. **265**: p. 1317-1324.
30. Paris, P.C., M.P. Gomez, and W.P. Anderson, *A rational analtyic theory of fatigue* The Trend in Engineering, 1961. **13**: p. 9-14.
31. Dubourg, M.-C. and V. Lamacq, *A predictive rolling contact fatigue crack growth model: Onset of branching, direction, and growth - Role of dry and lubricated conditions on crack patterns.* Transaction of the ASME - Journal of Tribology, 2002. **124**(4): p. 680-688.
32. Glodez, S., et al., *Numerical modelling of crack path in the lubricated rolling-sliding contact problems.* Engineering fracture mechanics, 2008. **75**(3-4): p. 880-891.
33. Wong, S.S.L., et al., *Fatigue crack growth rates under sequential mixed-mode I and II loading cycles.* Fatigue & fracture of engineering materials & structures, 2000. **23**(8): p. 667-74.
34. Zhao, P., et al., *Subsurface propagation of partial ring cracks under rolling contact: Part II. Fracture mechanics analysis.* Wear, 2006. **261**(3-4): p. 390-397.

Appendix A

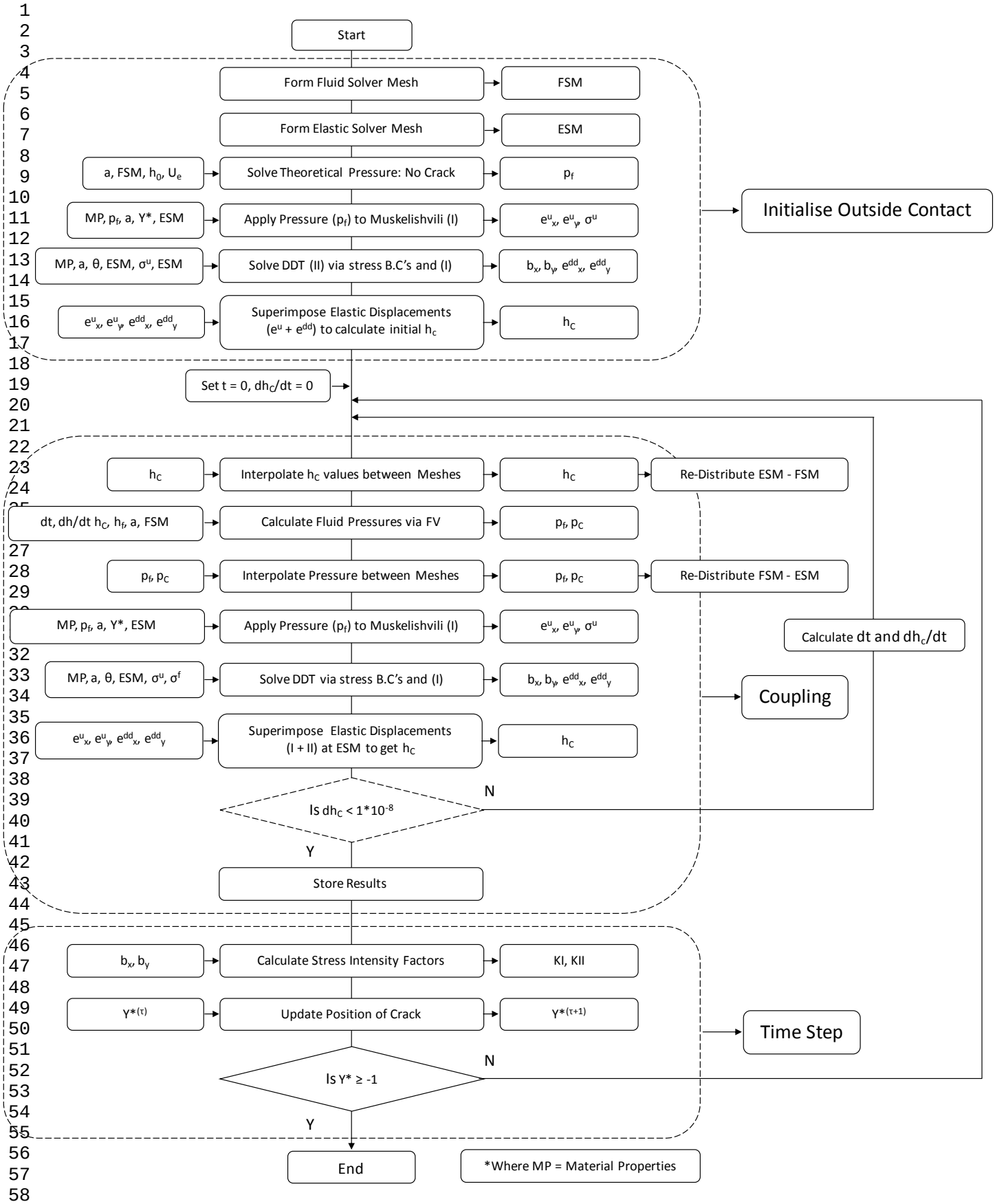

Figure A1 – Solution algorithm.

Captions to Figures and Tables

Figure 1 – Schematics: (a) the system under investigation and (b) the equivalent wedge geometry. In Figure 1(b) the finite volumes discretisation of the fluid domain is also shown.

Figure 2 – Overall problem and schematic describing the fluid and solid solvers and their components.

Figure 3 – Layout of the computational Finite Volume domain.

Figure 4 – Distributed dislocation: schematic of the distribution of glide and climb dislocations and of the normalised solution intervals (between –1 and 1).

Figure 5 – Validation of solvers and intermediate steps. (a) Comparison between FV and analytical solutions for the pressure distribution at the contact interface; the half-Sommerfeld solution is also shown to demonstrate the validity of the wedge approximation for development purposes. (b) Comparison between the normalised volumetric fluxes at the crack mouth computed using the FV solver and the crack volume changes due to the elastic deflections (integrated over the crack length). (c) Comparison between the crack deflections computed using the DDT and the FEM package ANSYS for a pressurised crack benchmark problem.

Figure 6 – (a) Contour plot showing the evolution of the crack opening displacements. (b) “Slices” through the contour plot in Figure 6(a) showing the evolution of the crack opening at three locations within the crack.

Figure 7 – Crack shape at three instants in time immediately before closure.

Figure 8 – Evolution of the crack mouth opening vs. (a) the volumetric flux at the crack mouth, and (b) the pressure gradient at the crack mouth during one loading cycle.

Figure 9 – Evolution of the normalised volumetric flux at the crack mouth for the example cases in Table 1.

Figure 10 – Evolution of the normalised stress intensity factors for the example cases in Table 1: (a) Mode I, and (b) Mode II.

Figure 11 – Comparison of the evolution of the normalised stress intensity factors predicted by the present coupled finite volume (CFV) approach, a Squeeze Oil Film (SOF) model, an uncoupled fluid pressure model (FPM), and an uncoupled tapered pressure model (TPM) from the literature for Case 2 in Table 1: (a) Mode I, and (b) Mode II.

Figure A1 – Solution algorithm.

Table 1 – Example problems parameters.

Figures

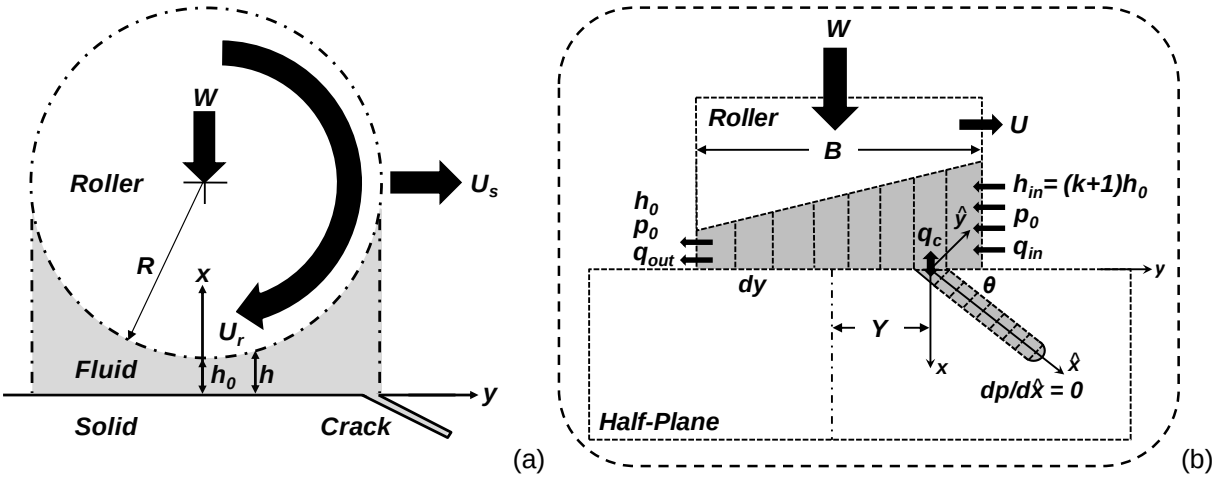

Figure 1 – Schematics: (a) the system under investigation and (b) the equivalent wedge geometry. In Figure 1(b) the finite volumes discretisation of the fluid domain is also shown.

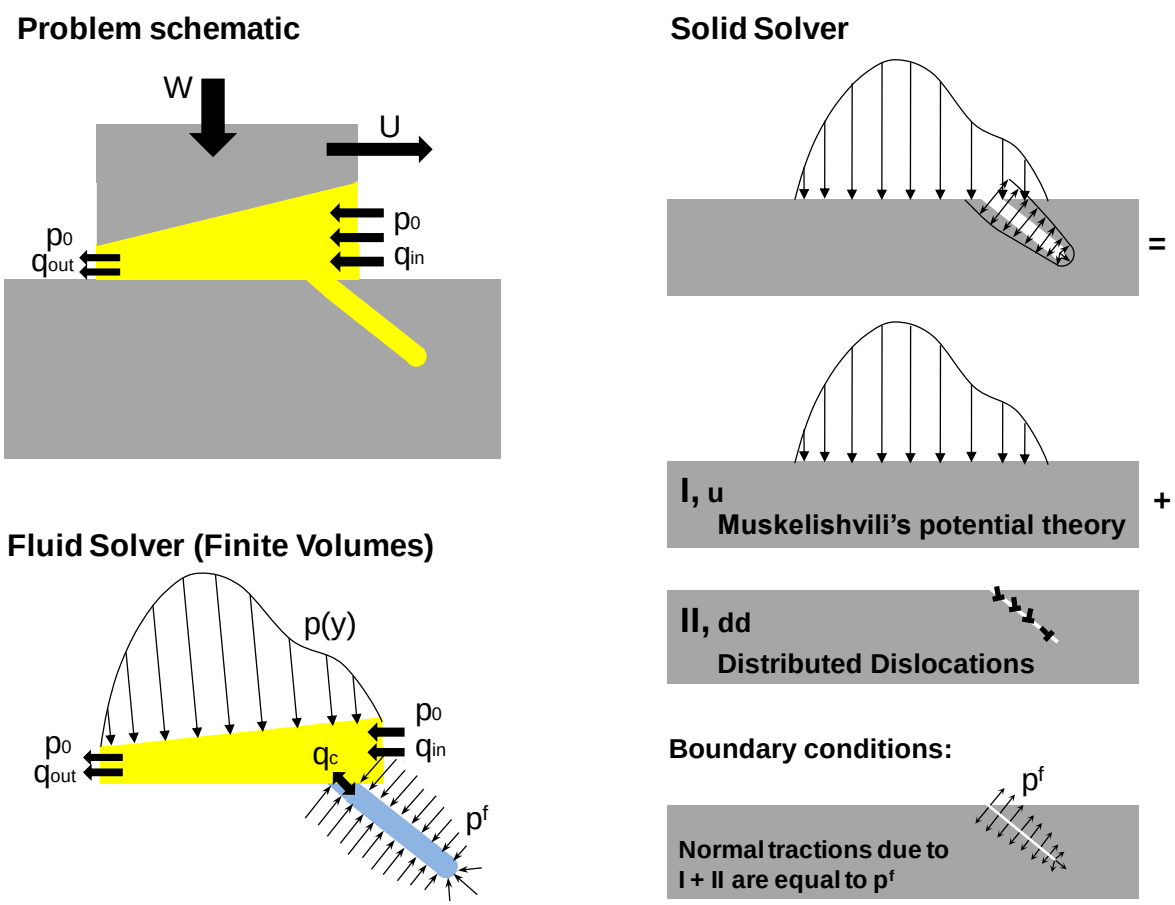

Figure 2 – Overall problem and schematic describing the fluid and solid solvers and their components.

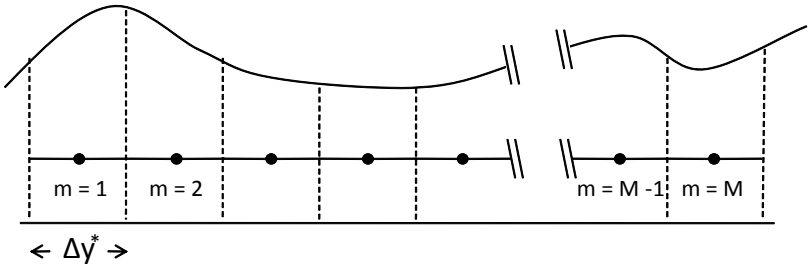

Figure 3 – Layout of the computational Finite Volume domain.

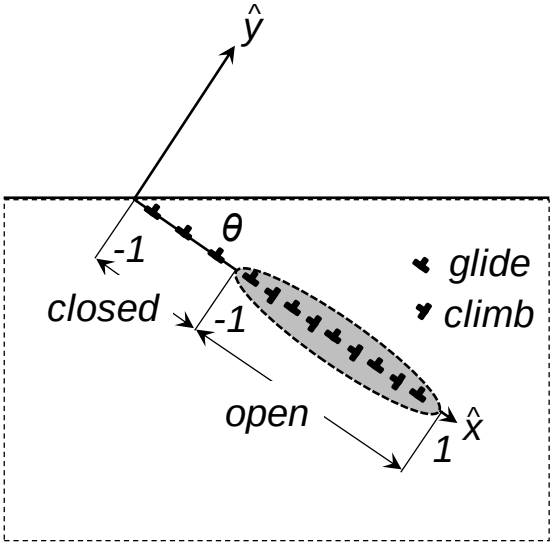

Figure 4 –Distributed dislocation: schematic of the distribution of glide and climb dislocations and of the normalised solution intervals (between *–1* and *1*).

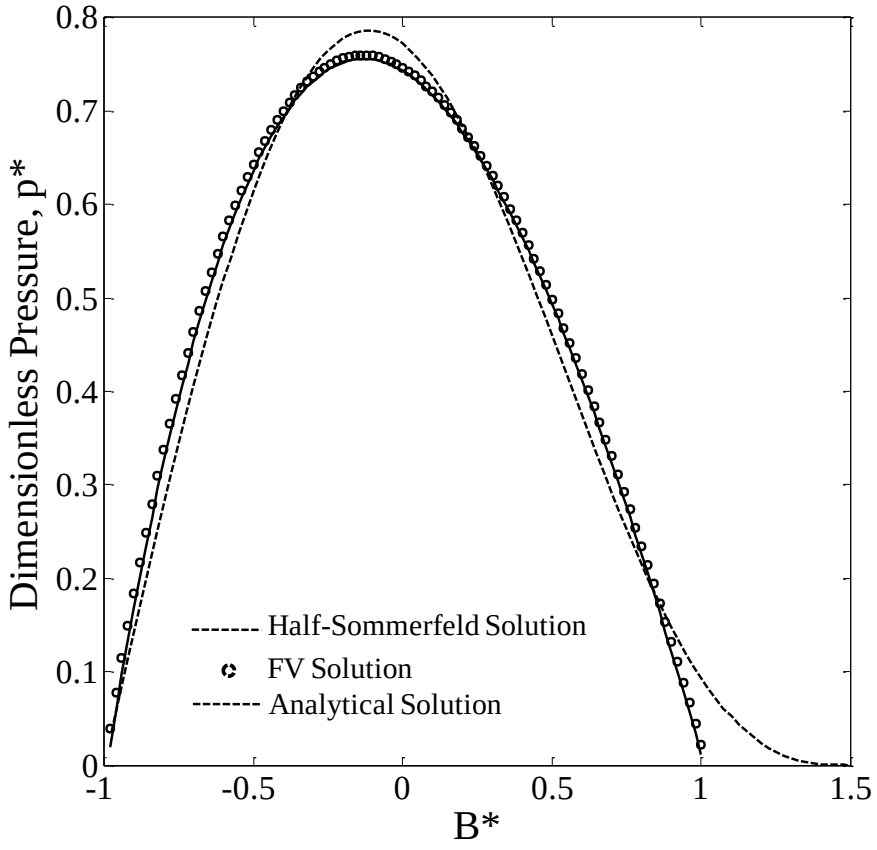
Dimensionless Pressure, p*
B*
Half-Sommerfeld Solution
FV Solution
Analytical Solution

(a)

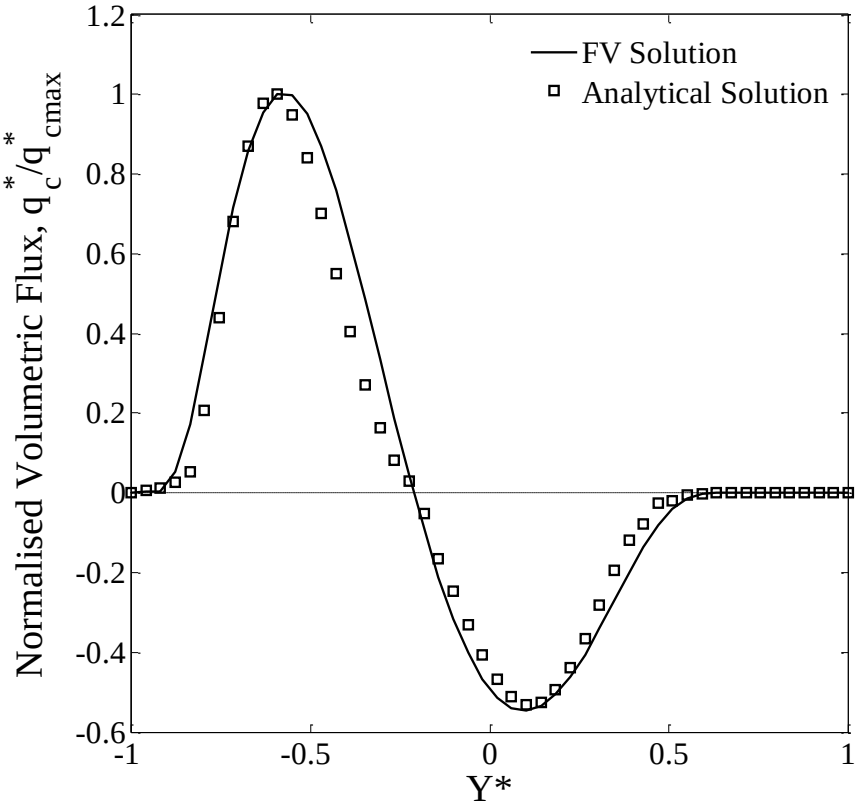
Normalised Volumetric Flux, q*c/q*cmax
Y*
FV Solution
Analytical Solution

(b)

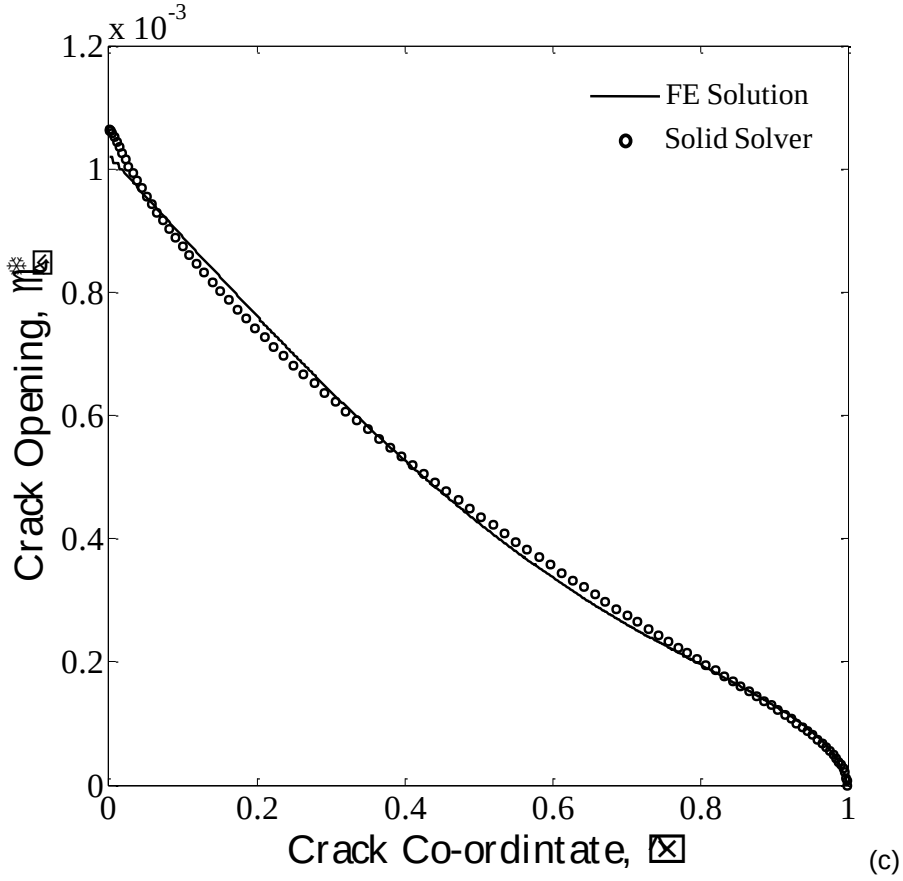

Figure 5 – Validation of solvers and intermediate steps. (a) Comparison between FV and analytical solutions for the pressure distribution at the contact interface; the half-Sommerfeld solution is also shown to demonstrate the validity of the wedge approximation for development purposes. (b) Comparison between the normalised volumetric fluxes at the crack mouth computed using the FV solver and the crack volume changes due to the elastic deflections (integrated over the crack length). (c) Comparison between the crack deflections computed using the DDT and the FEM package ANSYS for a pressurised crack benchmark problem.

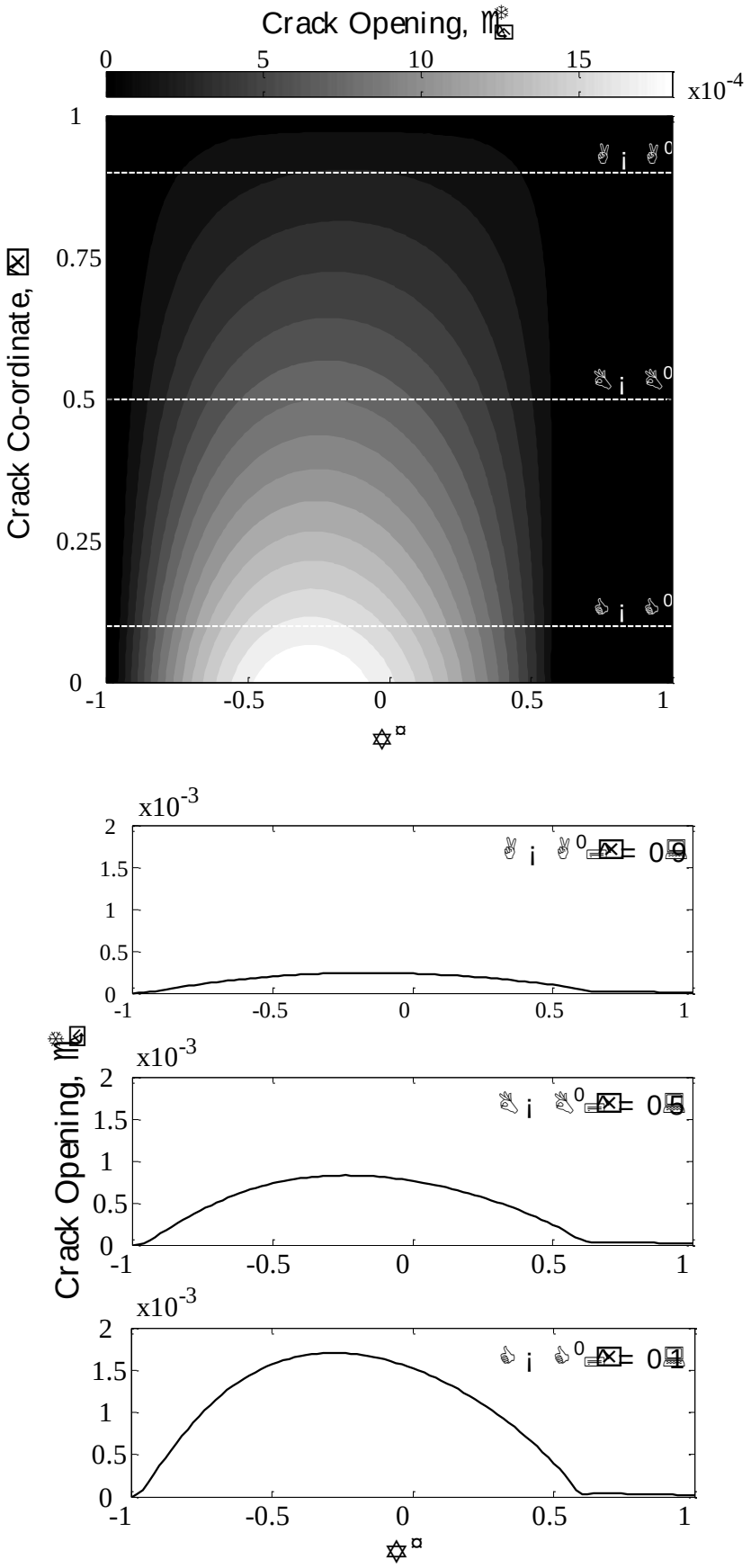

Figure 6 – (a) Contour plot showing the evolution of the crack opening displacements. (b) "Slices" through the contour plot in Figure 6(a) showing the evolution of the crack opening at three locations within the crack.

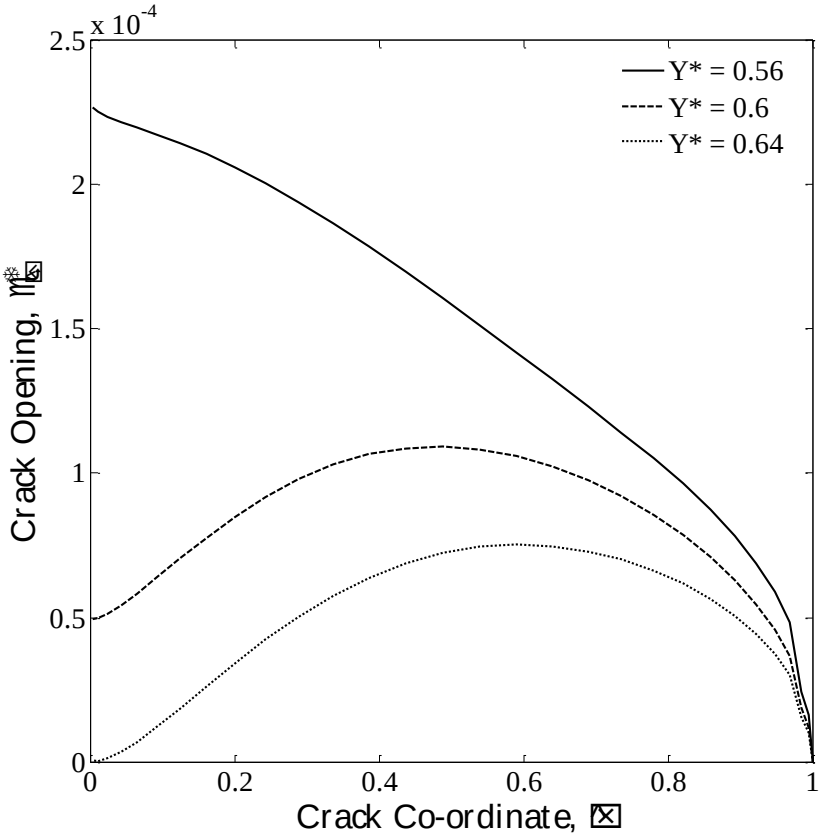

Figure 7 – Crack shape at three instants in time immediately before closure.

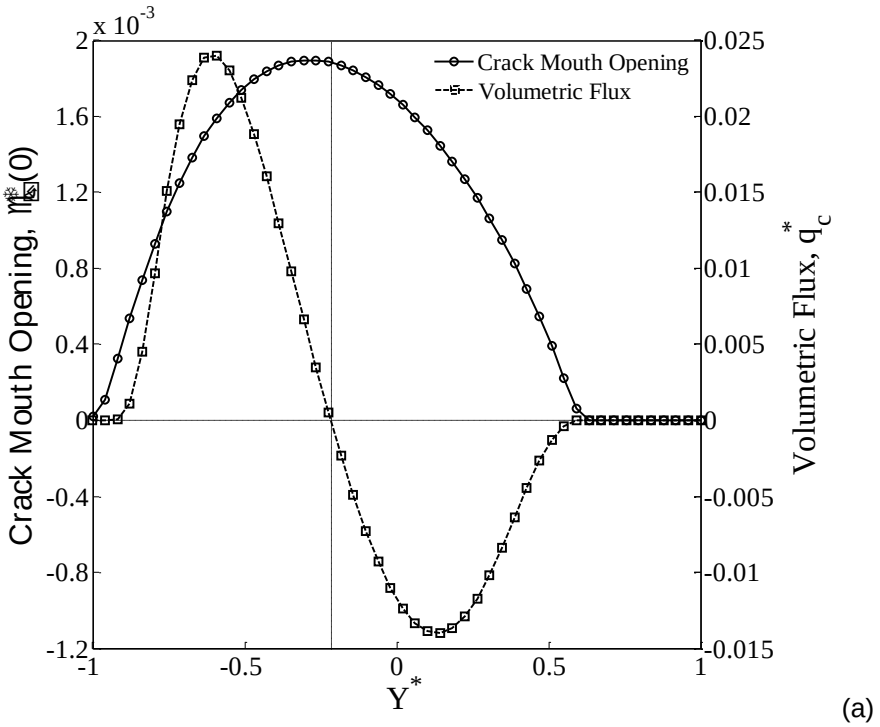

(a)

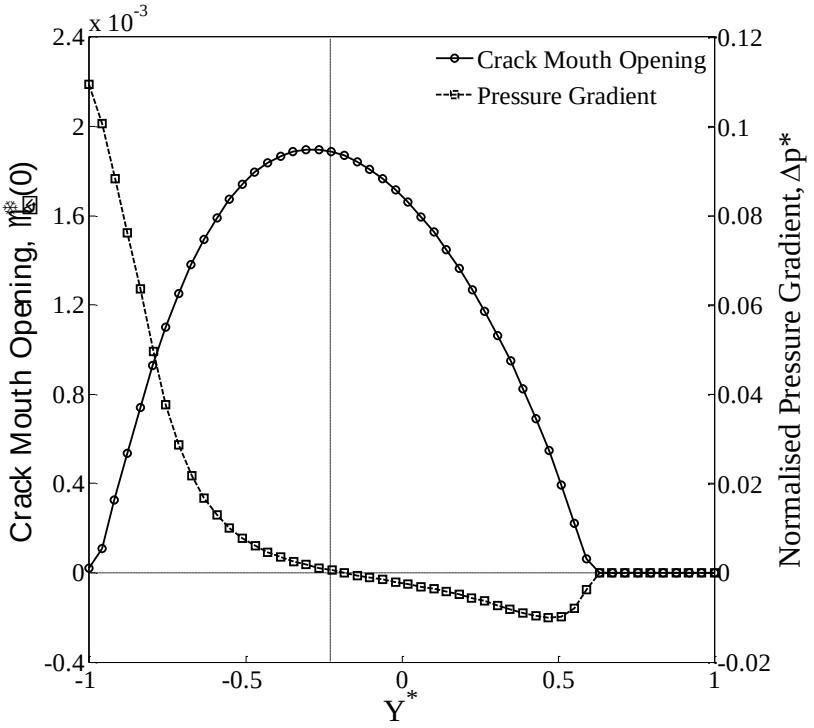

Figure 8 – Evolution of the crack mouth opening vs. (a) the volumetric flux at the crack mouth, and (b) the pressure gradient at the crack mouth during one loading cycle.

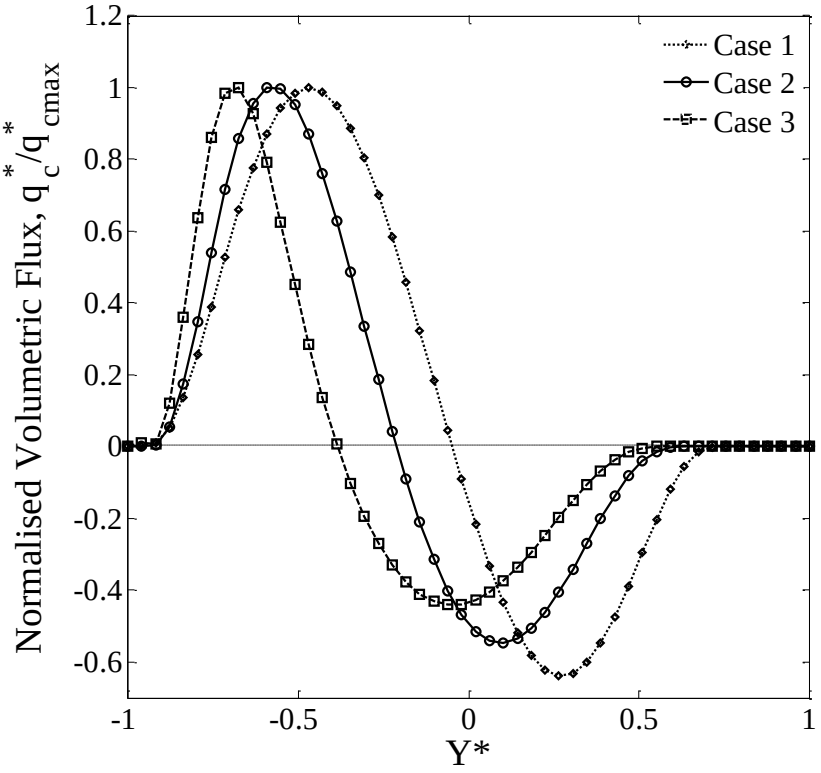

Figure 9 – Evolution of the normalised volumetric flux at the crack mouth for the example cases in Table 1.

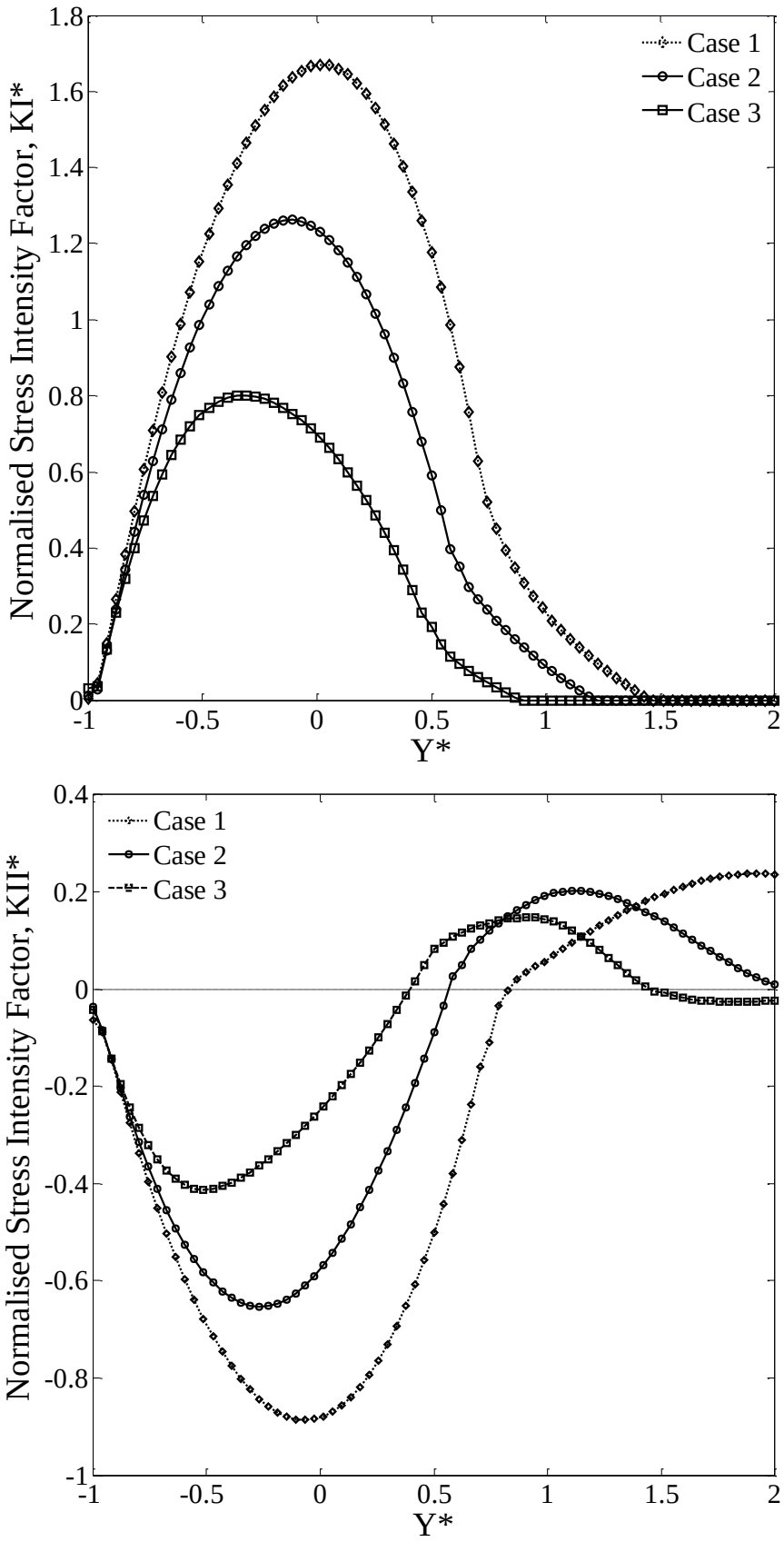

Figure 10 – Evolution of the normalised stress intensity factors for the example cases in Table 1: (a) Mode I, and (b) Mode II.

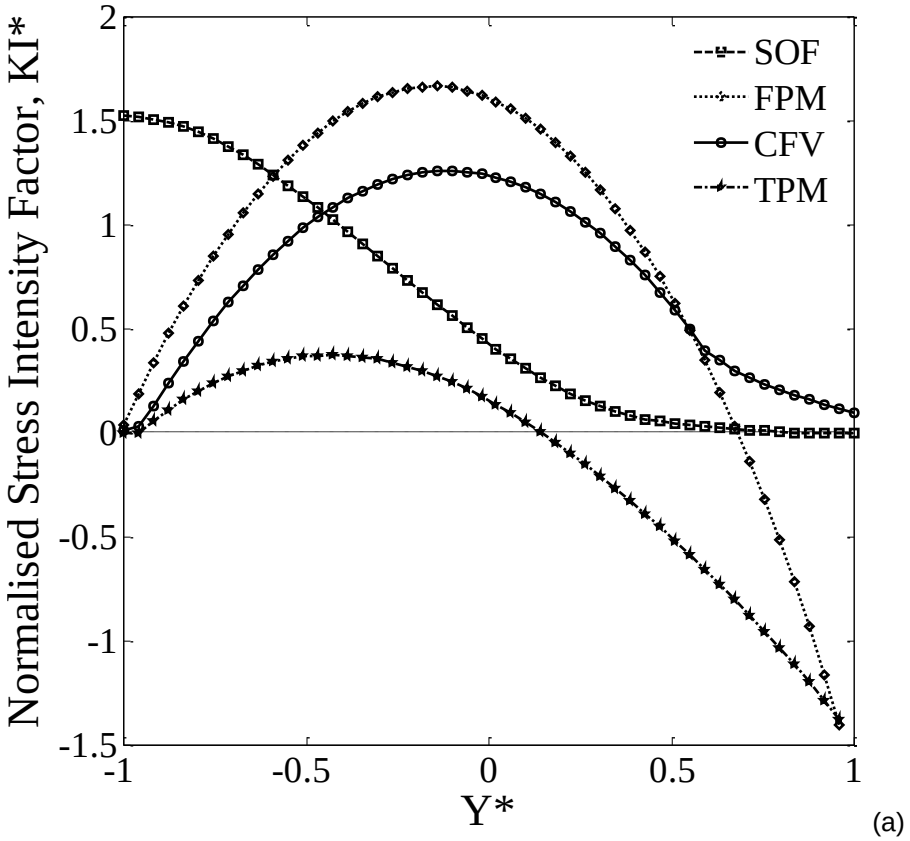

(a)

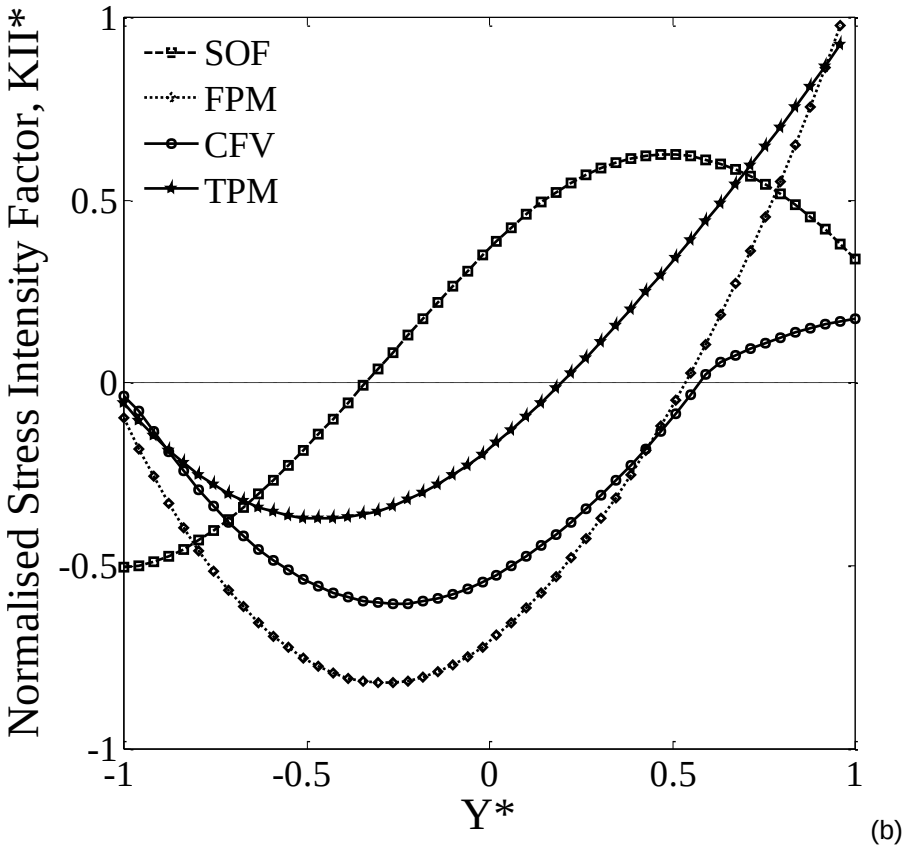

(b)

Figure 11 – Comparison of the evolution of the normalised stress intensity factors predicted by the present coupled finite volume (CFV) approach, a Squeeze Oil Film (SOF) model, an uncoupled fluid pressure model (FPM), and an uncoupled tapered pressure model (TPM) from the literature for Case 2 in Table 1: (a) Mode I, and (b) Mode II.

Tables

Case	Liquid	a	B	h_0	U_S	W_F	E	σ_Y	η	θ	k
		μm	μm	nm	m/s	N/m	GN/m^2	MN/m^2	Pa/s	°	
1	Base Oil	200	200	152	0.2	5000	210	800	0.137	25	0.325
2	Base Oil	100	200	152	0.2	5000	210	800	0.137	25	0.325
3	Base Oil	50	200	152	0.2	5000	210	800	0.137	25	0.325

Table 1 – Example problems parameters.